SEARCH FOR THE TOP QUARK IN $\overline{p}p$ COLLISIONS AT $\sqrt{s} = 1.8$ TEV

John J. Walsh

A DISSERTATION

in

PHYSICS

Presented to the Faculties of the University of Pennsylvania in Partial Fulfillment of the Requirements for the Degree of Doctor of Philosophy

1990

Hugh H. Williams

Supervisor of Dissertation

Graduate Group Chairperson

ACKNOWLEDGMENTS

I would like to thank Brig Williams and Pekka Sinervo for their many contributions to this top quark search. They contributed greatly to the analysis and also helped me very much in producing this thesis. A number of people of the CDF Heavy Flavour Group have also contributed to this analysis, and I thank them for their effort and assistance. Finally, I thank my fellow CDF collaborators and the technical staff at Fermilab, who have made this experiment and accelerator a great success.

ABSTRACT

SEARCH FOR THE TOP QUARK IN $\overline{p}p$ COLLISIONS AT $\sqrt{s} = 1.8$ TEV

John J. Walsh

Dissertation Supervisor: H. H. Williams

A search for the top quark in $\overline{p}p$ collisions at a center of mass energy of 1.8 TeV using the Collider Detector at Fermilab is described. A study of events selected by requiring an energetic electron, missing transverse energy, and two or more jets excludes at 95% confidence level the Standard Model production and decay of $t\bar{t}$ pairs if the top quark mass is between 40 and 77 GeV/c^2. The observed electron + multijet data are consistent with W boson production.

Contents

1 Introduction **1**

1.1 Experimental evidence for the top quark 1

1.1.1 Electroweak interactions 2

1.1.2 Forward-backward asymmetry 4

1.1.3 Rare b decays 7

1.2 Top quark production and decay 9

1.3 Theoretical assumptions 13

2 The Detector and the Data **15**

2.1 The CDF detector 15

2.1.1 Tracking 15

2.1.2 Calorimetry 17

2.2 Trigger system 20

2.3 Data collection 21

2.4 Monte Carlo data sets 22

3 Event Selection **25**

3.1 Inclusive electron selection 25

3.1.1 Selection criteria 25

3.1.2 Removal of conversion electrons 30

3.1.3 Efficiencies and backgrounds 36

3.2 Electron + jets selection for Top 41

3.2.1 Isolation 43

3.2.2 Z^0 removal 45

3.2.3 Jets 47

3.3 Kinematic cuts - final sample 54

3.3.1 "Loose" and "Tight" E_T and $\not\!\!E_T$ cuts 54

3.3.2 Backgrounds in the final sample 57

4 Transverse Mass Analysis **66**

4.1 Transverse mass 66

4.1.1 Measuring and modeling transverse mass 66

4.1.2 Fitting transverse mass 70

4.2 Systematic uncertainties 75

4.2.1 Systematic uncertainties in determining α 76

4.2.2 Systematic uncertainties in normalization 81

4.3 Top mass limit 83

5 Conclusions **94**

5.1 Consistency with indirect constraints 94

5.1.1 $B^0\bar{B}^0$ mixing 95

5.1.2 Neutral current data and vector boson masses 97

5.2 Future prospects 101

6 Bibliography **103**

List of Figures

1.1 Lowest order diagrams for top quark production in $\bar{p}p$ collisions. . . . 11

1.2 Cross section for top quark production in $\bar{p}p$ collisions at $\sqrt{s} = 1.8$ TeV. 12

1.3 Top quark decay diagrams. 12

2.1 Elevation view of the CDF detector. 16

2.2 One module of the central calorimeter. 19

3.1 Distribution of variables used in electron identification. 29

3.2 Variables used to identify conversions. 32

3.3 Scatterplot of $\not{E}_T$ vs E_T^{em} for the inclusive electron sample. 42

3.4 Electron and leading and non-leading jet E_T for inclusive electrons. . 44

3.5 Electron isolation variable E_T^{iso}. 46

3.6 Mass spectrum of di-electron candidates. 48

3.7 Jet detection efficiency. 51

3.8 Pseudorapidity distribution of jets from $t\bar{t}$ and W + 2 jet events. . . . 53

3.9 Scatterplot of $\not\!\!E_T$ vs E_T^{em} for events with an electron and two or more jets. 55

3.10 $\not\!\!E_T$ vs E_T^{em} scatterplot for background events. 56

3.11 Scatterplot of $M_T^{e\nu}$ vs $p_T^{e\nu}$ for the electron + 2 jet data sample. 62

3.12 $M_T^{e\nu}$ and $p_T^{e\nu}$ for electron + 2 jet data. 63

3.13 Comparison of electron + 2 jet data with W + 2 jet Monte Carlo data. 64

4.1 Monte Carlo distributions of $M_T^{e\nu}$ for top quarks and for W + 2 jet events. 67

4.2 Transverse mass for electron + 1 jet events. 69

4.3 Fit contours in α, β space. 74

4.4 Normalized likelihood distributions from the transverse mass fits. . . 86

4.5 Smeared likelihood distributions from the transverse mass fits. 88

4.6 The 95% C.L. upper limit for the $t\bar{t}$ production cross section as a function of top mass. 93

5.1 Box diagrams contributing to $B^0\bar{B}^0$ mixing 95

5.2 Effect of electroweak measurements on the top quark mass. 99

List of Tables

1.1 Standard model neutral current couplings. 4

3.1 Cuts used in the electron selection. 28

3.2 Summary of conversion analysis for inclusive electrons. 35

3.3 Summary of electron efficiency analysis. 38

3.4 Summary of numbers used to calculate the charged pion background in the inclusive electron sample. 40

3.5 Summary of jet cuts. 52

3.6 Efficiency of kinematic cuts as a function of M_{top}. 58

3.7 Summary of numbers used to calculate the non-isolated electron background in the electron + 2 jet sample. 59

3.8 Conversion efficiency and background as a function of electron E_T. . . 60

3.9 Summary of non-electron background for final sample of electron + 2 jet events. 61

4.1 Transverse mass fit results. 75

4.2 Systematic variation of fitted $t\bar{t}$ fraction α. 78

4.3 Systematic variations in α for $M_{top} = 70$ GeV/c^2. 79

4.4 Summary of $\Delta\alpha$ for systematic effects for which the $M_T^{e\nu}$ distribution must be refit. 80

4.5 Summary of systematic uncertainties in overall normalization. 84

4.6 Summary of numbers used to calculate the upper limit on the $t\bar{t}$ production cross section. 89

4.7 Check of confidence level for the observed $t\bar{t}$ cross section. 91

5.1 Dependence of radiative corrections, Δr, on the top quark mass. . . . 98

Chapter 1

Introduction

This paper describes a search for the top quark in $\overline{p}p$ collisions at $\sqrt{s} = 1.8$ TeV. The result of this analysis, that a top quark with mass (M_{top}) in the range $40 < M_{top} < 77$ GeV/c^2 is excluded at 95% confidence level, has been published previously [1]; the purpose of this paper is to provide the details of that analysis. At the time this search was undertaken, searches for t quarks at e^+e^- machines had yielded a lower limit of 28 GeV/c^2 on the top quark mass [2]. Searches for t quark production and decay in $\overline{p}p$ collisions at $\sqrt{s} = 630$ GeV had placed a lower limit on the top quark mass of 41 GeV/c^2 at 95% confidence level (C.L.) [3, 4]. Recent results have extended those limits to 44.5 GeV/c^2 and 69 GeV/c^2 at 95% C.L. for e^+e^- and $\overline{p}p$ searches, respectively [5].

1.1 Experimental evidence for the top quark

Given the negative results of top quark searches to date, it is worthwhile reviewing the evidence that indicates the top quark does indeed exist. After a very brief summary

of the Standard Model electroweak Lagrangian, we discuss two experimental results that are difficult to interpret if the top quark does not exist.

1.1.1 Electroweak interactions

The standard model of electroweak interactions has been described in detail elsewhere [6], we review briefly the highlights necessary for this paper. The standard model electroweak sector is based on the $SU(2) \times U(1)$ gauge group. Forces are mediated by four gauge bosons, the massless photon and the massive $W^{\pm}$ and Z^0 bosons. Fermions are grouped into three generations of quarks and leptons, which, for the left-handed fields, transform as SU(2) doublets:

$$\begin{pmatrix} \nu_e \\ e^- \end{pmatrix} \begin{pmatrix} \nu_\mu \\ \mu^- \end{pmatrix} \begin{pmatrix} \nu_\tau \\ \tau^- \end{pmatrix} \quad \text{leptons}$$

$$\begin{pmatrix} u \\ d' \end{pmatrix} \begin{pmatrix} c \\ s' \end{pmatrix} \begin{pmatrix} t \\ b' \end{pmatrix} \quad \text{quarks}$$

where d', s', and b' represent the weak eigenstates of the down-type quarks. They are related to the mass eigenstates (d, s, and b) via

$$\begin{pmatrix} d' \\ s' \\ b' \end{pmatrix} = V \begin{pmatrix} d \\ s \\ b \end{pmatrix} \tag{1.1}$$

where V is the Cabbibo-Kobayashi-Maskawa (CKM) mixing matrix. The right-handed fields transform as SU(2) singlets. A neutral scalar, the Higgs boson, gives mass to the fermions and massive gauge bosons via spontaneous symmetry breaking.

The Lagrangian describing the interaction of the fermion fields with the gauge bosons (i.e. without the mass, self-interaction, or Higgs boson terms) may be written as

$$\mathcal{L}_G = \mathcal{L}_{em} + \mathcal{L}_{CC} + \mathcal{L}_{NC} \tag{1.2}$$

where the three terms correspond to electromagnetic, charged, and neutral currents, respectively. In terms of the fermion and gauge boson fields one has

$$\mathcal{L}_{em} = -e \sum_f Q_f \bar{f} \gamma^\mu f A_\mu, \tag{1.3}$$

$$\begin{aligned} \mathcal{L}_{CC} &= -\left(\frac{G_F M_W^2}{\sqrt{2}}\right)^{1/2} \left[\bar{\nu}\gamma^\mu(1-\gamma_5)eW_\mu^+ + \bar{e}\gamma^\mu(1-\gamma_5)\nu W_\mu^- \right. \\ &+ \left. \bar{u}\gamma^\mu(1-\gamma_5)d'W_\mu^+ + \bar{d}'\gamma^\mu(1-\gamma_5)uW_\mu^- + \cdots \right] \end{aligned} \tag{1.4}$$

and

$$\mathcal{L}_{NC} = -\sqrt{2}\left(\frac{G_F M_Z^2}{\sqrt{2}}\right)^{1/2} \sum_f \left[c_L^f \bar{f}\gamma^\mu(1-\gamma_5)f + c_R^f \bar{f}\gamma^\mu(1+\gamma_5)f\right] Z_\mu \tag{1.5}$$

where f represents a general fermion field, u represents the u quark field, etc., e in Eq. (1.3) is the electric charge of the positron, Q_f is the electric charge of the fermion, G_F is the Fermi constant, A_μ, $W_\mu^\pm$, and Z_μ represent the four gauge boson fields and M_W and M_Z are the masses of the W and Z bosons. The coupling constants for the

Table 1.1: Standard model neutral current couplings.

	$\nu_e,\ \nu_\mu,\ \nu_\tau$	$e,\ \mu, \tau$	$u,\ c,\ t$	$d,\ s,\ b$
Q_f	0	-1	$+2/3$	$-1/3$
c_L	$\frac{1}{2}$	$-\frac{1}{2}+\sin^2\theta_W$	$\frac{1}{2}-\frac{2}{3}\sin^2\theta_W$	$-\frac{1}{2}+\frac{1}{3}\sin^2\theta_W$
c_R	0	$\sin^2\theta_W$	$-\frac{2}{3}\sin^2\theta_W$	$\frac{1}{3}\sin^2\theta_W$
v	1	$-1+4\sin^2\theta_W$	$1-\frac{8}{3}\sin^2\theta_W$	$-1+\frac{4}{3}\sin^2\theta_W$
a	1	-1	1	-1

neutral current, c_L and c_R, are shown in Table 1.1. One observes from the electroweak Lagrangian that at tree-level quark decays occur only via the charged current. This is a consequence of the absence of flavor changing neutral currents in the Standard Model.

1.1.2 Forward-backward asymmetry

Perhaps the most compelling evidence that the b quark belongs to an SU(2) doublet, and hence that the top quark exists, comes from the measured forward-backward charge asymmetry in the reaction $e^+e^- \to b\bar{b}$. The spin averaged differential cross section, using the Born approximation and neglecting final state masses and QCD corrections is given by [7]

$$\begin{aligned}\frac{4s}{\alpha^2}\frac{d\sigma}{d\Omega}(e^+e^- &\rightarrow f\bar{f}) \\ &= \frac{1}{4}\left[|Q_f - 8c_L^e c_L^f g(s)|^2 + |Q_f - 8c_R^e c_R^f g(s)|^2\right](1+\cos\theta)^2 \quad (1.6) \\ &+ \frac{1}{4}\left[|Q_f - 8c_L^e c_R^f g(s)|^2 + |Q_f - 8c_R^e c_L^f g(s)|^2\right](1-\cos\theta)^2\end{aligned}$$

where θ is the angle between the incoming electron and the outgoing fermion in the center of mass system, and

$$g(s) = \frac{G_F}{\sqrt{2}}\frac{M_Z^2}{4\pi\alpha}\left(\frac{s}{s - M_Z^2 + iM_Z\Gamma_Z}\right). \quad (1.7)$$

Here Γ_Z is the width of the Z^0 boson, s is square of the center of mass energy, and α is the fine structure constant. Equation (1.6) can be expressed as a sum of symmetric and antisymmetric terms

$$\frac{4s}{\alpha^2}\frac{d\sigma}{d\Omega}(e^+e^- \rightarrow f\bar{f}) = C_S(1+\cos^2\theta) + 2C_A\cos\theta \quad (1.8)$$

with

$$C_S = Q_f^2 - Q_f v_e v_f \mathrm{Re}\{g(s)\} + \frac{1}{4}(v_e^2 + a_e^2)(v_f^2 + a_f^2)|g(s)|^2 \quad (1.9)$$

and

$$C_A = -Q_f a_e a_f \mathrm{Re}\{g(s)\} + v_e v_f a_e a_f |g(s)|^2. \quad (1.10)$$

The v_i and a_i are the vector and axial vector charges

$$\begin{aligned} v_i &= 2(c_L^i + c_R^i) \quad (1.11) \\ a_i &= 2(c_L^i - c_R^i). \end{aligned}$$

The standard model values are given in Table 1.1.

The forward-backward asymmetry is defined as

$$A_{FB} \equiv \frac{\int_0^1 \frac{d\sigma}{d\cos\theta}\, d\cos\theta - \int_{-1}^0 \frac{d\sigma}{d\cos\theta}\, d\cos\theta}{\int_0^1 \frac{d\sigma}{d\cos\theta}\, d\cos\theta + \int_{-1}^0 \frac{d\sigma}{d\cos\theta}\, d\cos\theta}. \tag{1.12}$$

Integration of Eq. (1.8) yields

$$A_{FB} = \frac{3}{4}\frac{C_A}{C_S} \tag{1.13}$$

$$\simeq -\frac{3}{4}\frac{a_e a_f}{Q_f}\mathrm{Re}\{g(s)\}, \quad \text{for } s \ll M_Z^2. \tag{1.14}$$

The JADE collaboration has reported [8] an asymmetry measurement for $e^+e^- \to b\bar{b}$ at $\sqrt{s} = 34.6$ GeV. They tag events containing a b quark by selecting events with a prompt muon, and they further separate quark flavors on the basis of muon transverse momentum, missing transverse momentum, and jet transverse mass, where transverse means transverse to the jet axis. They report a measured value of the asymmetry:

$$A_{FB} = -(22.8 \pm 6.0 \pm 2.5)\%. \tag{1.15}$$

Assuming this energy and standard model couplings with $\sin^2\theta_W = .23$, Eq. (1.13) predicts an asymmetry of -27%. At this energy the mass of the b quark is not entirely negligible: its effect is to reduce the expected asymmetry to -25%. The corrections due to QCD effects are smaller than the mass corrections and are not considered here.

Assuming $a_e = -1$ and $Q_b = -1/3$ the JADE asymmetry measurement yields a value for the axial coupling of the b quark:

$$a_b = -.90 \pm 0.24 \pm .010, \tag{1.16}$$

consistent with the standard model prediction. In the presence of $B^0\bar{B}^0$ mixing, the value of A_{FB} is reduced. The ARGUS mixing result [9] implies that Eq. (1.14) should read

$$A_{FB} \simeq -(1-2\chi)\frac{3}{4}\frac{a_e a_f}{Q_f}\mathrm{Re}\{g(s)\}, \quad \text{for } s \ll M_Z^2 \tag{1.17}$$

where

$$\chi \equiv \frac{\Gamma(B^0 \to \bar{B}^0)}{\Gamma(B^0 \to \text{all})}. \tag{1.18}$$

The ARGUS measurement implies $(1-2\chi) = 0.78 \pm 0.08$, which takes into account the fact that the ARGUS result was for B_d mesons only. The JADE result for a_b is still consistent with the standard model, and the world average of of measurements for a_b, corrected for the presence of $B^0\bar{B}^0$ mixing, yields

$$a_b = -1.00 \pm 0.28 \tag{1.19}$$

which is in very good agreement with the standard model and strongly implies the existence of the top quark as the SU(2) partner of the b quark.

1.1.3 Rare b decays

The existence of the top quark is also implied by the non-observation of flavor changing neutral currents in b quark decays [10]. If the b quark is assumed to decay via the Standard Model gauge bosons, and if it is not a member of an SU(2) doublet, then b quark should decay via flavor-changing neutral currents. The charged and neutral

current terms of Eqs. (1.4) and (1.5) can be expressed in terms of the isospin triplet of the left-handed $(V-A)$ currents $(J^+_\mu, J^-_\mu, J^3_\mu)$:

$$\mathcal{L}_G = \mathcal{L}_{em} - \frac{g}{\sqrt{2}}(W^-_\mu J^{\mu+} + W^+_\mu J^{\mu-}) - \frac{g}{\cos\theta_W} Z_\mu (J^{\mu 3} - \sin^2\theta_W J^\mu_{EM}), \tag{1.20}$$

where $g = e/\sin\theta_W$ and J^μ_{EM} is the electromagnetic current. If the b quark is an SU(2) singlet, it can only only enter the Lagrangian (aside from the purely electromagnetic terms, which, because they are flavor diagonal, cannot mediate b decay) via Cabbibo mixing with the d and s quarks. In this case the currents may be written

$$J^+_\mu = \bar{u}\gamma^\mu \frac{(1-\gamma^5)}{2} d' + \bar{c}\gamma^\mu \frac{(1-\gamma^5)}{2} s', \tag{1.21}$$

$$\begin{aligned} J^3_\mu = \frac{1}{2}\Bigg(& \bar{u}\gamma^\mu \frac{(1-\gamma^5)}{2} u + \bar{c}\gamma^\mu \frac{(1-\gamma^5)}{2} c \\ & - \bar{d}'\gamma^\mu \frac{(1-\gamma^5)}{2} d' - \bar{s}'\gamma^\mu \frac{(1-\gamma^5)}{2} s' \Bigg) \end{aligned} \tag{1.22}$$

where d' and s' are orthogonal linear combinations of the mass eigenstates d, s, and b. Expanding in terms of the mass eigenstates, one finds

$$J^+_\mu = \alpha_u \bar{u}\gamma^\mu \frac{(1-\gamma^5)}{2} b + \alpha_c \bar{c}\gamma^\mu \frac{(1-\gamma^5)}{2} b + \cdots \tag{1.23}$$

$$J^3_\mu = -\frac{1}{2}\alpha_d \bar{d}\gamma^\mu \frac{(1-\gamma^5)}{2} b - \frac{1}{2}\alpha_s \bar{s}\gamma^\mu \frac{(1-\gamma^5)}{2} b + \cdots \tag{1.24}$$

where the α_q are functions of the mixing angles. One may then compute the following ratio of widths for b decay:

$$\frac{\Gamma(B \to X\ell^+\ell^-)}{\Gamma(B \to X\ell^+\nu)} = \left[(\frac{1}{2} - \sin^2\theta_W)^2 + (\sin^2\theta_W)^2 \right] A, \tag{1.25}$$

where A is given by

$$A = \frac{\alpha_d^2 + \alpha_s^2}{\alpha_u^2 + P\alpha_c^2}, \tag{1.26}$$

and P is a phase space factor, $P \simeq 0.65$. The α_q are constrained by the measured values of $|V_{ud}|$ and $|V_{us}|$ and by the small observed value of the $K_L - K_S$ mass difference (i.e. by the absence of strangeness changing neutral current decays). The limit

$$A \geq 0.98 \tag{1.27}$$

is obtained, which includes the possibility of more than one singlet quark in the model. This constraint on A, combined with Eq. (1.25), yields

$$\frac{\Gamma(B \to X\ell^+\ell^-)}{\Gamma(B \to X\ell^+\nu)} \geq 0.12, \tag{1.28}$$

which must hold if the b quark is not a member of an SU(2) doublet. The CLEO collaboration has found [11]

$$BR(B \to X\ell^+\ell^-) < 1.2 \times 10^{-3} \tag{1.29}$$

at 90% confidence level. This corresponds to

$$\frac{\Gamma(B \to X\ell^+\ell^-)}{\Gamma(B \to X\ell^+\nu)} < 0.01, \tag{1.30}$$

which clearly violates Eq. 1.28, thereby implying the existence of the top quark.

1.2 Top quark production and decay

Top quarks can be produced directly through QCD processes resulting in a $t\bar{t}$ pair or they may be produced (if kinematically allowed) through W boson production

followed by the decay $W \rightarrow t\bar{b}$ (see Fig. 1.1). A theoretical prediction of the t quark cross section in $\bar{p}p$ collisions at $\sqrt{s} = 1.8$ TeV [4] for both of these processes is shown in Fig. 1.2. Direct $t\bar{t}$ pair production is the dominant source of top quarks for all top masses.[1] We therefore concentrate on the detection of t quarks produced in $t\bar{t}$ pairs. Figure 1.3 shows the diagrams for hadronic and semileptonic decays of the top quark. The Standard Model branching ratio for the semileptonic decay is 1/9 for each lepton species. The branching ratio for the hadronic decay (summed over quark species) is 2/3. For this analysis, we will consider the decay mode where one t quark decays semileptonically and the other hadronically. Assuming a the Standard Model branching ratios for the top quark, this signature comprises about 15% of the $t\bar{t}$ rate for each lepton species considered. The fully hadronic decay modes have the highest rate (about 44% of the $t\bar{t}$ rate), but the background from QCD multijet production is very high. Requiring two leptons in the final state is a very clean signal for $t\bar{t}$ events, but the rate is low (e.g., the branching fraction for $t\bar{t} \rightarrow e\mu X$ is $\sim 2.5\%$). The analysis described here requires the presence of a high-p_T electron plus missing transverse energy plus hadronic jets as a signal for $t\bar{t}$ production. The reaction, then, that we consider is

[1] This contrasts the situation at the CERN $\bar{p}p$ collider where the decay of W bosons is an important potential source of top quarks.

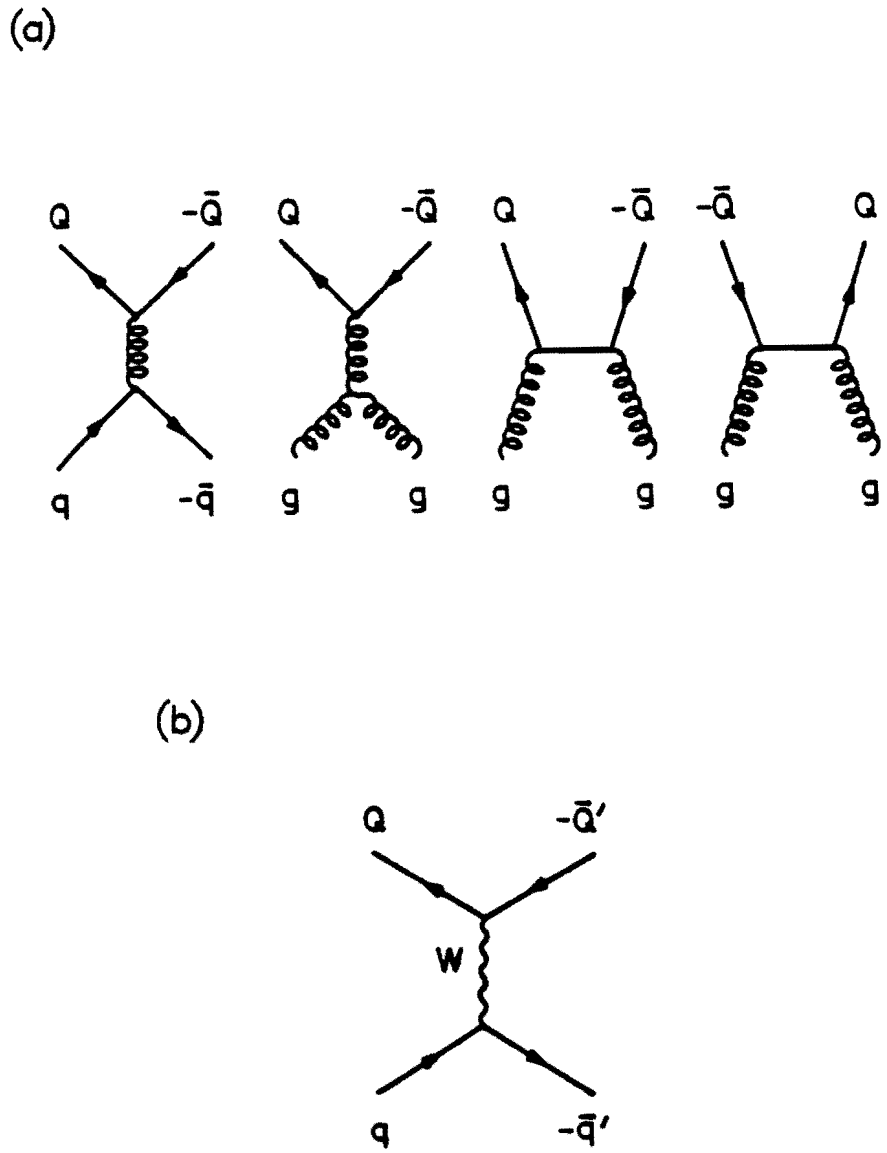

Figure 1.1: Lowest order diagrams for top quark production in $\bar{p}p$ collisions: (a) direct $t\bar{t}$ pair production, (b) top quark production via W decay.

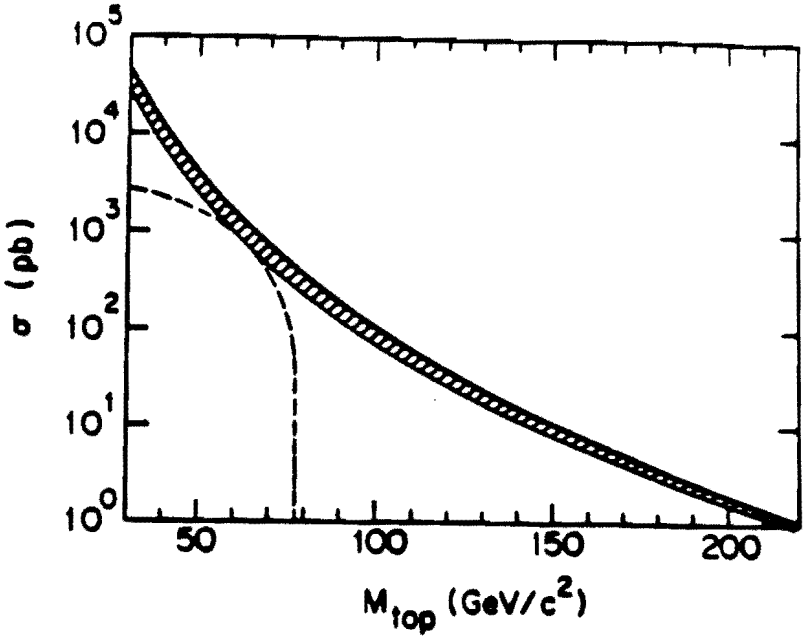

Figure 1.2: Cross section for top quark production in $\bar{p}p$ collisions at $\sqrt{s} = 1.8$ TeV. The solid curve is for $t\bar{t}$ pair production, the dashed curve for $W \rightarrow t\bar{b}$.

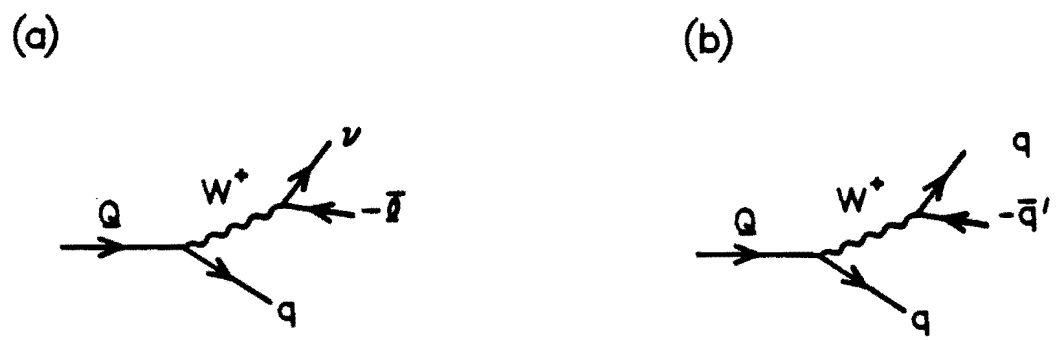

Figure 1.3: Top quark decays diagrams, (a) semileptonic, (b) hadronic.

$$\overline{p}p \rightarrow t\bar{t} + X$$
$$\hookrightarrow \bar{b}q\bar{q}'$$
$$\hookrightarrow be^{+}\nu$$

The CDF collaboration has also reported on a top quark search using the $e\mu$ signature [12].

1.3 Theoretical assumptions

This report presents results on the upper limit of the observed $t\bar{t}$ cross section, from which a limit on the top quark mass is derived. The limit on the cross section depends on the Standard Model semileptonic branching ratio of 1/9 for top quarks. In particular, this cross section upper limit relies on the prediction that the decay $t \rightarrow b + W$ (virtual or real) is dominant. If a charged scalar H^{+} exists with mass such that the decay $t \rightarrow b + H^{+}$ is kinematically allowed, then the branching ratio of $t \rightarrow be\nu$ can be greatly suppressed [13]. This would reduce the sensitivity of any top quark search that requires the t quark to decay semileptonically into an electron or a muon. A derivation of a limit on the mass of the top quark from the measured upper limit on $t\bar{t}$ production is sensitive to the theoretical prediction of the cross section for that process. The $t\bar{t}$ production cross section used to determine a limit on the top

quark mass is discussed in Sec. 2.4.

Chapter 2

The Detector and the Data

2.1 The CDF detector

The Collider Detector at Fermilab (CDF) is a general purpose magnetic detector situated at the Tevatron collider at Fermilab. An elevation view of the CDF detector is presented in Fig. 2.1. The detector has been described in detail elsewhere [14]; here we describe the components relevant to this analysis.

2.1.1 Tracking

A set of eight time projection chambers mounted around the beam pipe provide r-z tracking[1] to a radius of 22 cm from the beam in the pseudorapidity[2] region $|\eta| < 3.5$. This vertex time projection chamber (VTPC) presents less than 2% of a radiation length of material to tracks with $|\eta| < 1.5$. In this analysis a primary function of the

[1] In the CDF coordinate system z is measured from the center of the detector along the proton beam, y is measured vertically, and x is measured horizontally. r is the perpendicular distance to the beam: $r = \sqrt{x^2 + y^2}$.

[2] Pseudorapidity is defined by $\eta \equiv -\ln(\tan\frac{\theta}{2})$, where θ is the angle measured from the proton beam.

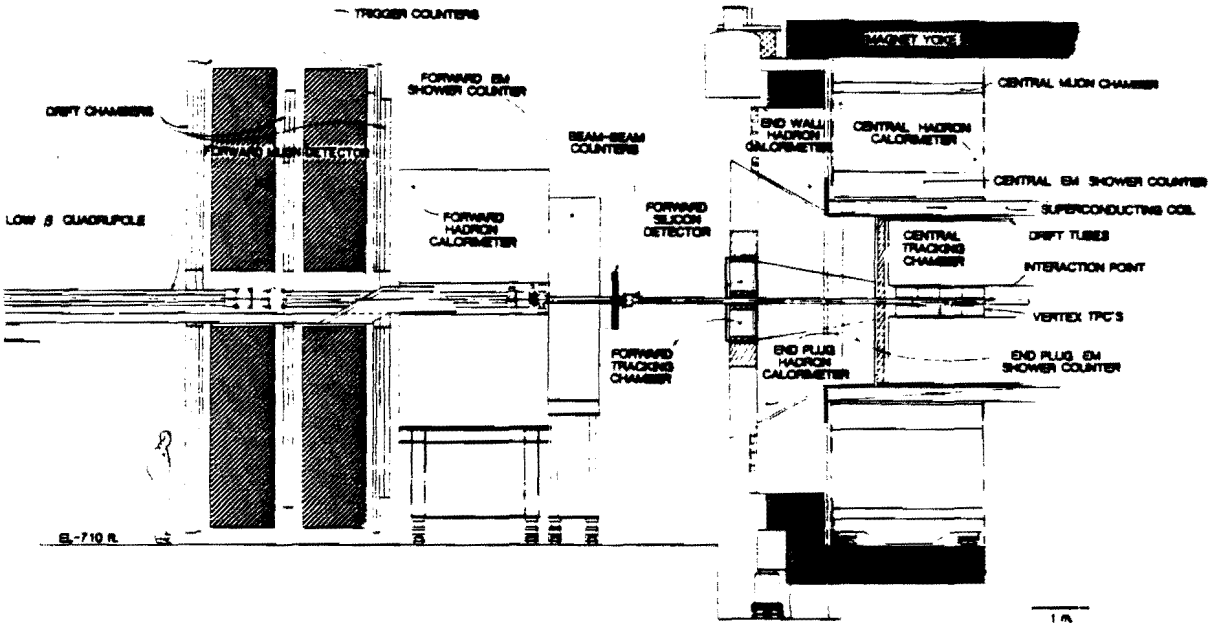

Figure 2.1: Elevation view of the CDF detector. The detector is forward-backward symmetric.

VTPC was to locate the event vertex along the beam axis. The resolution on this measurement is typically a few millimeters. Another function of the VTPC was to provide information used in the identification of photon conversions (see Sec. 3.1.2).

A large cylindrical drift chamber provides charged particle tracking in the region $|\eta| < 1.2$. This central tracking chamber (CTC) has 84 sense wire layers arranged in nine superlayers extending to a radius of 1.3 m. Twenty-four layers of sense wires are tilted 3° with respect to the beam direction to provide 3-dimensional stereo information. Operated in a 1.412 Tesla solenoidal magnetic field, the CTC transverse momentum resolution is $\delta p_T/{p_T}^2 = 0.0017\ (GeV/c)^{-1}$. The resolution is improved to $\delta p_T/{p_T}^2 = 0.0011\ (GeV/c)^{-1}$ by constraining track trajectories to pass through the beam position [15].

2.1.2 Calorimetry

The CDF calorimeter is divided into three sections of pseudorapidity, called the central, plug, and forward regions, providing coverage over the region $|\eta| < 4.2$. Each section consists of an electromagnetic calorimeter and a hadronic calorimeter. In this analysis the central region ($|\eta| < 1.1$) was used for primary electron identification. Jets were detected in the central and plug calorimeters, whereas the full calorimeter out to $|\eta| < 3.6$ was used to calculate missing transverse energy, $\not{E}_T$.

A lead-scintillator sampling calorimeter 18 radiation lengths deep provides elec-

tromagnetic shower detection in the region $|\eta| < 1.1$. This central electromagnetic calorimeter (CEM) is segmented into 15° wedges in the azimuthal direction, with each wedge consisting of twenty projective towers, each subtending $\sim .11$ units of pseudorapidity. Figure 2.2 shows a wedge of the central calorimeter.

The CEM was calibrated in an electron test beam to an accuracy of 2%, using electrons with momenta between 10 and 50 GeV/c. Cesium sources are used to track the energy calibration during running periods. The energy resolution for electrons is given by $\sigma(E)/E = 13.5\%/\sqrt{E_T} \oplus 1.7\%$ ($E_T \equiv E \sin\theta$ expressed in GeV, the terms are added in quadrature).

A set of proportional wire chambers is located in the CEM at a depth of six radiation lengths to measure the position and shape of electromagnetic showers. These central strip chambers (CES) have wire and cathode strip readout providing independent reconstruction of showers in the z (along the beam) and azimuthal views. The resolution on the position of shower centroids is about 2.5 mm for 25 GeV/c electrons.

Measurement of hadronic energy in the central region is provided by the central hadronic calorimeter (CHA). The CHA has approximately the same geometry and segmentation as the CEM and covers the same region of pseudorapidity ($|\eta| < 1.1$). The energy resolution is approximately $\sigma(E)/E = 80\%/\sqrt{E_T}$. The CHA photomultiplier tubes are instrumented with TDC's that provide timing information used to

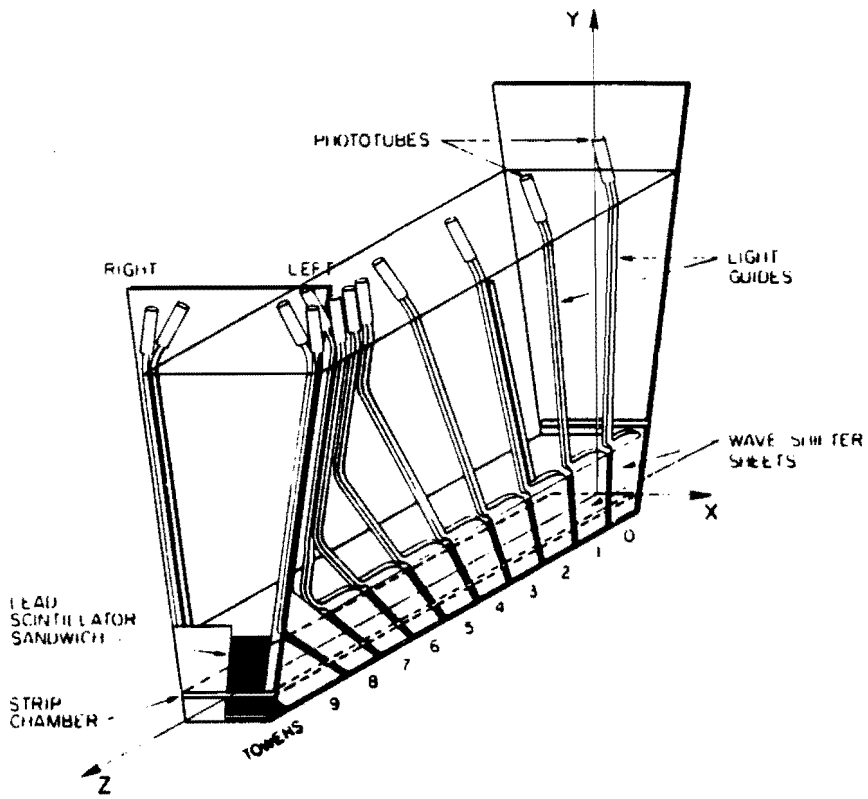

Figure 2.2: One module of the central calorimeter.

reject out-of-time backgrounds, such as cosmic rays or particles from the Tevatron's main ring, which passes over the detector.

The plug and forward calorimeters extend the calorimetric coverage to $|\eta| < 4.2$. These are gas sampling calorimeters with cathode pad readout. They are segmented into projective towers of size $\Delta\eta \times \Delta\phi \sim 0.09 \times 0.087$, and are for this analysis used for jet energy measurements and for total E_T and $\not{E}_T$ measurements. The energy resolution for the gas calorimeters is approximately $\sigma(E)/E = 30\%/\sqrt{E_T}$ and $\sigma(E)/E = 100\%/\sqrt{E_T}$, for the electromagnetic and hadronic compartments, respectively.

2.2 Trigger system

The CDF trigger system is a three-level FASTBUS-based system of hardware processors and a "farm" of processors running algorithms written in high-level languages. We discuss here the parts of the trigger relevant to the current analysis. The level-0 trigger consists of a set of scintillation counters located at $3.2 < |\eta| < 5.9$, which is used to detect inelastic $\overline{p}p$ interactions. The level-1 trigger decision is based on energy deposited in the calorimeters. Towers are ganged together to form trigger towers with $\Delta\eta \times \Delta\phi \sim 0.2 \times 0.2$ uniformly over the entire calorimeter. A level-2 trigger cluster finder forms clusters of calorimetric energy and links them with high-p_T CTC tracks found by a hardware track processor. The level-3 trigger applies more sophisticated

algorithms to improve background rejection. For example, level-3 algorithms perform clustering using the full granularity of the calorimeter, perform CTC tracking in the r-ϕ view, and reconstruct electron showers in the strip chambers.

Inclusive electron trigger

The events used in this analysis were required to pass an inclusive electron trigger. The level-1 electron trigger requires at least 6 GeV of transverse energy in a single tower in the central region. The level-2 trigger requires an electromagnetic (EM) cluster in the central region with $E_T > 12$ GeV, with the ratio of hadronic to EM energy, $had/em < 0.125$. A CTC track pointing to the cluster (in the r-ϕ view) with $p_T > 6$ GeV/c is also required. In level-3, "noise" in the calorimeter system is removed and energy clustering is redone with the full calorimeter segmentation. The lateral energy profile of the electron candidate cluster is required to be consistent with an electron shower. Details of the electron clustering and lateral profile measurement can be found below in Sec. 3.1.1. This trigger has been measured to be $98 \pm 0.5\%$ efficient for electrons passing the offline selection criteria described in Sec. 3.1.1.

2.3 Data collection

The data set for this analysis was obtained during a one-year run of the Tevatron in 1988 and 1989. An event sample corresponding to an integrated luminosity of 4.4 pb^{-1}

was collected, corresponding to about 5 million recorded events. The uncertainty of the integrated luminosity is estimated to be $\pm 15\%$. A fast offline pre-filter reduced this sample by a factor of about twenty by imposing loose electron cuts. The major reduction was obtained by the requirement of a track with p_T of at least 10 GeV/c pointing at the electron cluster. The selection criteria described below further reduced this sample by another factor of about 2500.

2.4 Monte Carlo data sets

We discuss in this section the Monte Carlo data sets to which we will refer in subsequent sections. Monte Carlo event samples were generated for $t\bar{t}$, b and c quark, and W + jet production processes. All Monte Carlo events were passed through a full simulation of the CDF detector, including effects such as cracks, electronic noise, photon conversions, detector resolution, etc. After simulation, the events are passed through the offline reconstruction in the same way as the real data. The same event selection criteria were then applied to the reconstructed events, except for an algorithm which rejects electrons coming from photon conversions (see Sec. 3.1.2). The effect of this algorithm on prompt electrons has been calculated and the Monte Carlo efficiencies have been corrected accordingly.

The ISAJET [16] Monte Carlo program was used to generate $t\bar{t}$ events for top masses (M_{top}) of 40, 50, 60, 70, 75 and 80 GeV/c^2. The integrated luminosities of

the $t\bar{t}$ samples were 3.6, 3.6, 7.0, 13.0, 44.1, and 21.9 pb^{-1} for these event samples, respectively. For the $t\bar{t}$ production cross section we used the calculation by Altarelli *et al.* [4]. This calculation is based on the QCD total cross section formulas for heavy quark production, complete through order α_s^3, by Nason *et al.* [17].

ISAJET was also used to generate a sample of b and c quark events. All species of partons are included in this calculation, although requiring an electron with $p_T > 10$ GeV/c^2 in the event effectively selects only semileptonic decays of b and c quarks. Production of b quarks via the mechanisms of (i) direct $b\bar{b}$ production, (ii) gluon splitting, and (iii) flavor excitation are included in this calculation. Because this calculation is very CPU intensive, it is not practical to generate many inverse picobarns of $b\bar{b}$ data. The sample generated for this analysis corresponds to an integrated luminosity of 600 nb^{-1}.

The ISAJET program does reproduce well the jet activity in $W^{\pm}$ and Z^0 events. For this reason the PAPAGENO [18] program was used to generate events for the process $p\bar{p} \rightarrow W + \text{jets} + X$. PAPAGENO uses a W + n jets calculation [19], which includes tree-level diagrams for all relevant $2 \rightarrow 2$ and $2 \rightarrow 3$ processes. The partons generated by PAPAGENO are fragmented into hadrons following the method employed by ISAJET, using fragmentation parameters that have been adjusted to agree with CDF tracking data. An underlying event is generated using a modified version of the model used by ISAJET. The E_T scale of the underlying event was tuned to CDF data. The following

parameters were used to generate the W + 2 jet sample: (i) electron $p_T > 12$ GeV/c, (ii) parton $p_T > 8$ GeV/c, and (iii) $\Delta R \equiv \sqrt{(\Delta\eta)^2 + (\Delta\phi)^2} > .65$ between the two partons. The W + 2 jet sample corresponds to an integrated luminosity of 41.3 pb^{-1}, according to PAPAGENO's prediction for the cross section. We also generated a sample of W + 1 jet events, corresponding to an integrated luminosity of about 5 pb^{-1}.

Chapter 3

Event Selection

3.1 Inclusive electron selection

3.1.1 Selection criteria

Electron candidates are selected by requiring a cluster of electromagnetic energy associated with a CTC track in the central region. The energy cluster is required to have the correct shower profiles (both in the calorimeter and in the strip chambers) and the track must match the cluster both in position and momentum.

Before describing the details of the electron selection criteria, we describe the cluster algorithm used to define electron candidates. The electron cluster algorithm starts with "seed" towers with at least 3 GeV of electromagnetic transverse energy. Adjacent towers are added to the cluster if their $E_T > 0.1\ GeV$. In the central calorimeter an electron shower is generally contained within one or two towers. Furthermore, the border between towers in the ϕ direction contains roughly 1 cm of inactive material, which effectively prevents energy from a single shower crossing the ϕ boundary be-

tween towers in the central region. For these reasons, the size of central EM clusters is restricted to three or fewer towers in a single CEM wedge.

For the inclusive sample the electromagnetic cluster is required to have transverse electromagnetic energy, $E_T^{em} > 15\ GeV$. Real electrons are expected to have little leakage into the hadronic compartment of the calorimeter, so we impose the cut $had/em < 0.05$. We define a variable, $\mathcal{L}_{shr}$, which is a measure of the lateral shower profile for electron candidates in the central region:

$$\mathcal{L}_{shr} = 0.14 \sum_k \frac{M_k - P_k}{\sqrt{0.14^2 E + (\Delta P_k)^2}} \tag{3.1}$$

where the sum is over towers in the cluster adjacent to the seed tower, M_k is the measured energy in the adjacent tower, P_k is the expected energy in the adjacent tower, E is the electromagnetic energy in the cluster, and ΔP_k is an estimate of the error in P_k. The expected energy P_k is predicted using the the event vertex, the center of the shower as measured in the central strip chamber and a shower profile parametrization obtained from test beam measurements. The uncertainty in this quantity, ΔP_k, is taken to be the variation in P_k arising from a 1 cm shift in the center of the shower, while the first term in the denominator comes from the resolution of the central electromagnetic calorimeter. We impose the condition $\mathcal{L}_{shr} < 0.2$; the efficiency of this and the other electron selection criteria are discussed in Sec. 3.1.3 below.

Clusters of hits from the strip chambers locate the showers more precisely in

both the z and r-ϕ directions, and provide a detailed measurement of the shower profile. Electromagnetic showers are reconstructed independently in the two views of the strip chambers and the resulting profiles are fit to a parametrization of the profiles obtained from test beam electrons. The values of χ^2 obtained from the fits are required to satisfy $\chi^2_Z < 10$ and $\chi^2_\phi < 10$.

Requiring a track pointing at the electron candidate and imposing cuts on position and energy matching significantly reduce non-electron backgrounds. CTC tracks are extrapolated to the radius of the strip chambers and the extrapolated position is compared with the shower location defined by the strip clusters. The cuts $|\Delta z| < 3$ cm and $|\Delta x| < 1.5$ cm are made, where

$$\Delta z = z_{CES} - z_{CTC} \tag{3.2}$$

$$\Delta x = x_{CES} - x_{CTC} \tag{3.3}$$

and x is the distance from the wedge center in the azimuthal direction. The cut is tighter in the r-ϕ direction due to the better CTC resolution in that view. We impose an energy-momentum match between calorimeter cluster and CTC track by requiring the ratio of the energy in the cluster to the track momentum (E/p) to be less than 1.5.

Table 3.1 summarizes the electron cuts. Figure 3.1 shows distributions for some of the relevant variables. For each distribution cuts are made on all variables except the one being plotted.

Table 3.1: Cuts used in the electron selection.

Variable	Cut
E_T^{em}	> 15 GeV
had/em	< 0.05
$\mathcal{L}_{shr}$	< 0.2
χ_Z^2	< 10
χ_ϕ^2	< 10
Δz	< 3 cm
Δx	< 1.5 cm
E/p	< 1.5

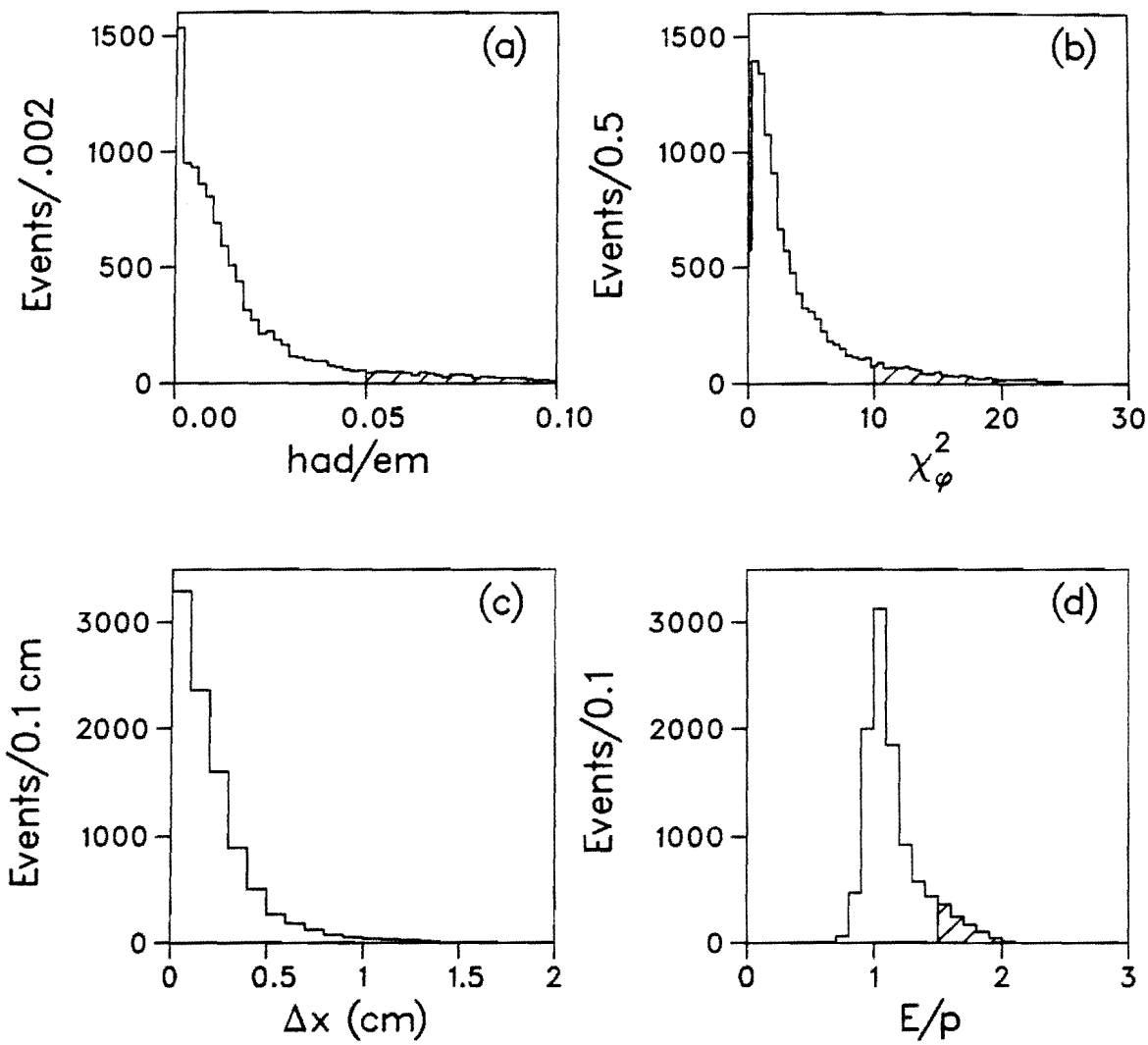

Figure 3.1: Distribution of variables used in electron identification. (a) had/em, (b) χ^2_ϕ, (c) Δx, (d) E/p. The shaded areas are cut.

We impose calorimeter fiducial cuts on the electron candidates to ensure that the electromagnetic shower is well measured. Electron candidates are required to be at least 2.5 cm from the ϕ-cracks between wedges of the central calorimeter and at least 9 cm away from a crack at $\theta = 90°$. Candidates that impact the outermost set of towers (at $\eta \sim \pm 1.1$) in the CEM calorimeter are also rejected, because for mechanical reasons these towers have fewer radiation lengths than the other CEM towers. Finally, an event is rejected if the z-coordinate of the primary vertex is more than 60 cm away from the center of the detector. This cut is made to insure that all jets are well contained in the calorimeters.

3.1.2 Removal of conversion electrons

A significant source of electrons are Dalitz decays of π^0's ($\pi^0 \rightarrow \gamma e^+ e^-$) and photons that interact in the material of the detector to produce an e^+e^- pair; we refer to both processes as "conversions." An electron arising from a conversion will usually be accompanied by a second track reconstructed in the CTC that forms a massless or nearly massless object with the electron candidate track. We form the pair mass for the electron candidate and all oppositely charged tracks within 30° of the candidate track, retaining the pair that results in the lowest mass. Figure 3.2(a) shows the invariant mass distribution of such track pairs for all electron candidates. The large peak near zero is indicative of conversions. Some conversions may also be identified by

considering the tracking information in the vertex chamber (VTPC). If a conversion occurs at a radius greater than that of the outer radius of the VTPC, there will be an absence of hits along the track path in the vertex chamber. Figure 3.2(b) shows the variable f_{VTPC}, defined as the number of VTPC hits found along the track path, divided by the number of hits expected. The excess at zero is due to conversions that occur outside the volume of the VTPC, which we will call "outer conversions". Conversions that occur inside the VTPC's inner radius, and therefore leave hits in the VTPC, will be called "inner conversions". Electrons arising from conversions are removed by rejecting electron candidates for which

$$m_{e^+e^-} < 0.5 \text{ GeV/c}^2 \quad \text{or} \quad f_{VTPC} < 0.2. \tag{3.4}$$

Outer conversions are removed by both the f_{VTPC} cut and the $m_{e^+e^-}$ cut. Inner conversions leave a track in the VTPC and therefore can only be removed by the mass cut.

We extract from the data: (i) the fraction of good electrons removed by the cuts, f_{prompt}; (ii) the efficiency of removing real conversions, ϵ_{conv}; and (iii) the fraction of the final sample attributed to unidentified conversions, f_{bg}. The analysis depends on the observation that any track passing through the VTPC will leave at least 20% of the expected hits, i.e., no good electron will be rejected by the f_{VTPC} cut. This has been verified by studying a sample of electrons from Z^0 decays. The second observation is that all "outer" conversions will fail the f_{VTPC} cut, i.e., they will be

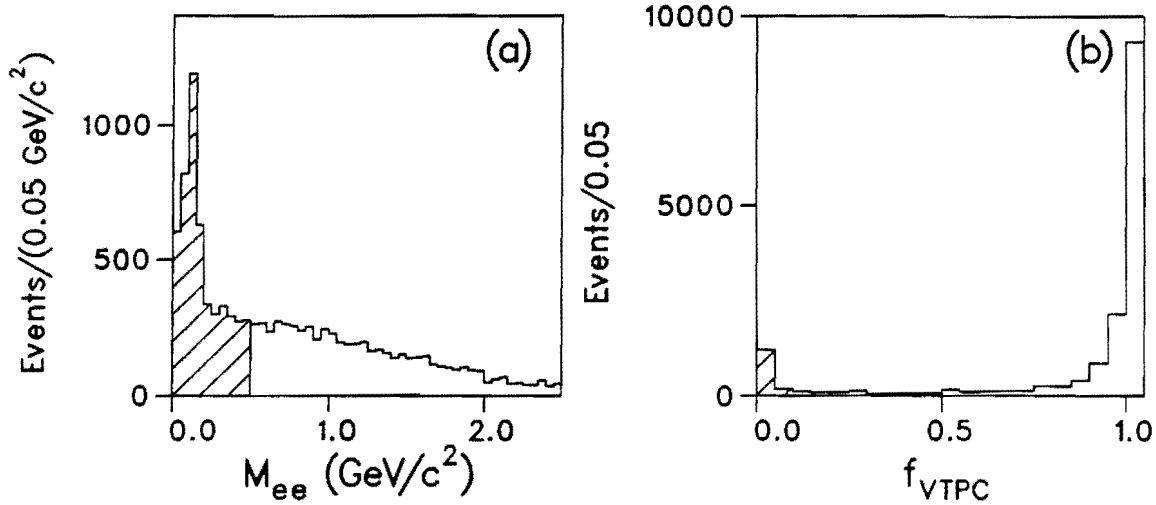

Figure 3.2: Variables used to identify conversions. (a) Invariant mass of electron candidate with a nearby track, (b) f_{VTPC}, fraction of expected hits observed in the VTPC along the electron direction. The events falling in the shaded regions are rejected.

identified by this cut. Thus the outer conversions form a sample of electrons that result entirely from photon conversions in the material surrounding the VTPC.

The fraction of prompt electrons removed by the cuts, f_{prompt}, is equal to the probability that a high-p_T electron candidate track together with a second uncorrelated track forms a pair mass less than 0.5 GeV. We have estimated this probability by considering how often like-sign pairs of tracks result in a low pair mass. This estimate can be written as

$$f_{prompt} = \frac{n_{i,ls}}{n_{i,ele}}, \tag{3.5}$$

where $n_{i,ls}$ is the number of electron candidates that have $f_{VTPC} > 0.2$ and $m_{e^+e^-} <$ 0.5 GeV/c^2, using pairs of like-sign tracks. The denominator, $n_{i,ele}$, is the total number of electron candidates with $f_{VTPC} > 0.2$. We find $f_{prompt} = 0.101$.

To determine the efficiency of the conversion removal criteria, we estimate the number of real conversions removed by the cuts and the total number of real conversions in the sample. Because the VTPC cut is essentially fully efficient with no over efficiency, we address the performance of the mass cut. The number of real conversions removed by the mass cut is given by

$$n_{ir} = n_i - n_{i,ls} \tag{3.6}$$

where n_i is the number of inner conversion candidates ($f_{VTPC} > 0.2$) and $n_{i,ls}$, defined above, is an estimate of the number of prompt electrons removed by the mass cut. The efficiency of the mass cut (i.e., the fraction of real inner conversions removed by

the mass cut) is determined from the sample of outer conversions identified by the VTPC cut:

$$\epsilon_{mass} = \frac{n_{o,m}}{n_o}, \tag{3.7}$$

where $n_{o,m}$ is the number of outer conversions that pass the $m_{e^+e^-}$ cut (i.e., the conversions that pass both cuts) and n_o is the number of outer conversions.

The number of real conversions identified by the cuts is then given by

$$n_{found} = n_o + n_{ir} \tag{3.8}$$

and the total number of real conversions in the sample is given by

$$n_{tot} = n_o + \frac{n_{ir}}{\epsilon_{mass}}. \tag{3.9}$$

The efficiency for removing conversions is then

$$\epsilon_{conv} = \frac{n_{found}}{n_{tot}} = 0.885. \tag{3.10}$$

The estimated number of conversion electrons remaining in this sample is given by

$$n_{bg} = (1 - \epsilon_{conv}) \times n_{tot}, \tag{3.11}$$

yielding 495 conversions; hence the fraction of the final sample attributed to unidentified conversions is $f_{bg} = 0.044$. A summary of the results of the conversion analysis is presented in Table 3.2.

Table 3.2: Summary of conversion analysis for inclusive electrons. The uncertainties shown are statistical.

Electron candidates	16598
Conversions candidates removed	5323
w/ $f_{VTPC} < 0.2$	1604
w/ $f_{VTPC} > 0.2$	3719
Number of conversions passing both cuts	1310
Estimate of prompt electrons removed	1512
Conversion removal efficiency, ϵ_{conv}	0.885 ± 0.029
Conversions as fraction of final sample, f_{bg}	0.044 ± 0.013
Fraction of prompt electrons removed, f_{prompt}	0.101 ± 0.002

3.1.3 Efficiencies and backgrounds

Electron selection efficiency

We determine the electron selection efficiency using Monte Carlo data and a sample of electrons from Z^0 decays in the data. The sample of Z^0 events is selected by requiring an electron candidate passing the selection criteria plus another electromagnetic cluster in the central region such that the pair form a mass between 80 and 105 GeV/c^2. We also require the first electron to satisfy $E_T^{em} > 20\ GeV$. The second cluster must have $E_T^{em} > 20$ GeV and a track pointing to it with $p_T > 10$ GeV/c. Finally, a very loose isolation cut is placed on both electrons to reduce any remaining background,

$$E_T^{cone} - E_T^{em} < 12\ GeV, \tag{3.12}$$

where E_T^{cone} is the energy in a cone of radius 0.4 in η–ϕ space, centered on the electron cluster. The electron efficiency is determined by measuring the number of second electrons that pass the selection. If N_Z is the number of Z^0's in the sample and N_2 is the number of second electrons that pass the cuts, then the efficiency of the cuts is given by

$$\epsilon = \frac{2\,N_2}{N_Z + N_2}. \tag{3.13}$$

The efficiency for a single cut (ϵ_c) is given by

$$\epsilon_c = \frac{\epsilon}{2}\left(1 - \frac{N_c}{N_Z}\right) + \frac{N_c}{N_Z}, \tag{3.14}$$

where ϵ is given in Eq. (3.13) above and N_e is the number of second electrons which pass the cut in question. The results of this analysis are presented in Table 3.3. We also show in Table 3.3 the results obtained from a Monte Carlo sample of $Z^0 \rightarrow e^+e^-$ events. There is good agreement between the data and Monte Carlo sample in all cases except perhaps for the efficiency of the E/p cut. In particular, the agreement in the overall efficiency is good. A similar study using electrons from $W^\pm$ decays yielded consistent results.

Backgrounds in the inclusive electron sample

Non-electron background in the electron sample comes primarily from photon conversions and from charged pions that deposit nearly all of their energy in the electromagnetic compartment of the calorimeter. We have found that backgrounds from charged pions overlapping a neutral electromagnetic shower from a π^0 or a photon are negligible.

Electrons arising from photon conversions and the Dalitz decay $\pi^0 \rightarrow \gamma e^+e^-$ are removed from the sample as discussed above (see Sec. 3.1.2). The remaining conversion background is estimated to be $4.4 \pm 1.3\%$ of the inclusive sample (see Table 3.2).

Charged pions whose showers are contained in the electromagnetic compartment of the calorimeter form the other significant background to electrons. We estimate

Table 3.3: Summary of electron efficiency analysis. The uncertainties shown are statistical only.

	Data		Monte Carlo	
N_Z	109		374	
N_2	68		229	
ϵ	$.768 \pm .032$		$.760 \pm .017$	
Single Cut Efficiencies				
Cut	N_c	ϵ_c	N_c	ϵ_c
had/em	104	.972	364	.983
E/p	93	.910	355	.969
$\mathcal{L}_{shr}$	105	.977	342	.947
Δx	105	.977	366	.987
Δz	107	.989	355	.969
χ^2_ϕ	84	.859	284	.851
χ^2_Z	100	.949	348	.957

the size of this background by comparing the relative number of events that pass or fail the *had/em* cut after all the other electron cuts have been made. If the efficiencies for passing this cut are known for electrons and for charged pions, the background remaining after the cut is applied can be determined. Let, N_p and N_f be the number of events that pass or fail the *had/em* cut, respectively, and let ϵ_e and ϵ_π be the efficiency of the *had/em* cut for electrons and charged pions, respectively. Then we can determine the total number of real electrons, N_e, and real charged pions, N_π in the sample before the *had/em* cut is applied by solving the two equations:

$$N_p = \epsilon_e N_e + \epsilon_\pi N_\pi, \tag{3.15}$$

$$N_p + N_f = N_e + N_\pi. \tag{3.16}$$

The efficiency of the *had/em* cut ($had/em < 0.05$) for pions is $\epsilon_\pi = 0.57 \pm 0.05$, determined from test beam studies. The efficiency for electrons was determined by considering electrons selected by the conversion algorithm. We only consider conversion candidates which have $1 < E/p < 1.1$, to reduce the probability that the conversion electron is accompanied by an extra electron or photon. This is necessary because extra electromagnetic energy accompanying the conversion electron distorts the *had/em* distribution. The efficiency of the *had/em* cut for electrons is thus determined to be $\epsilon_e = .95 \pm .02$. This efficiency for the *had/em* cut is somewhat lower than that determined using Z^0 events (Sec. 3.1.3). This is due to the fact that in general conversion electrons are less isolated than electrons from Z^0 (or $W^\pm$) decay. In a

Table 3.4: Summary of numbers used to calculate the charged pion background in the inclusive electron sample.

Charged pion background calculation		
electron efficiency	ϵ_e	$0.95 \pm .02$
pion efficiency	ϵ_π	$0.57 \pm .05$
inclusive electron candidates	N_p	11157
events failing *had/em* cut only	N_f	2152
number of real electrons	N_e	9397 ± 986
number of real pions	N_π	3912 ± 979
background as % of sample	$f_{bg}^{\pm}$	20 ± 5

conversion event it is more likely that additional hadronic energy will accompany the electron's energy, thereby increasing the *had/em* ratio. Because the inclusive electron sample contains a significant number of electrons from Z^0 and $W^\pm$ decay, the amount of charged pion background calculated using the lower *had/em* efficiency will be a slight overestimate.

The size of the charged pion background expressed as a fraction of the inclusive electron sample is then

$$f_{bg}^{\pm} = \frac{\epsilon_\pi N_\pi}{N_p} = 20 \pm 5\%. \tag{3.17}$$

The details of the calculation are provided in Table 3.4.

In summary, we find the inclusive electron sample to contain backgrounds from photon conversions and charged pions of $4.4 \pm 1.3\%$ and $20 \pm 5\%$, respectively. The total non-electron background is estimated to be

$$f_{bg}^{tot} = 24 \pm 5\%. \tag{3.18}$$

3.2 Electron + jets selection for Top

It is instructive to consider the distribution of the electron transverse energy vs the missing transverse energy in the event, $\not{E}_T$. The missing E_T is defined by

$$\not{E}_T = \left|\vec{\not{E}}_T\right| = \left|-\sum_i E_{T_i}\hat{n}_i\right| \tag{3.19}$$

where E_{T_i} is the transverse energy in the ith calorimeter tower and $\hat{n}_i$ is a unit vector directed from the event vertex to the tower. The sum is over all calorimeter towers with $|\eta| < 3.6$. The scatterplot of $\not{E}_T$ vs E_T^{em} for the inclusive electron sample is shown in Fig. 3.3 (only about 2 pb^{-1} of data are shown for clarity). There is a large cluster of events with high E_T^{em} and high $\not{E}_T$, as expected for W events where $W \to e\nu$. Also, Z production is evident in the events with high E_T^{em} and low $\not{E}_T$. The majority of the inclusive electron events are clustered at low values of E_T^{em} and $\not{E}_T$, where one expects to find semileptonic decays of b and c quarks and fake electron events. All of these processes form backgrounds to a potential top signal. We discuss in this section the additional cuts used to define a top quark sample. The background from b and c quark production is reduced by imposing an isolation requirement on electrons.

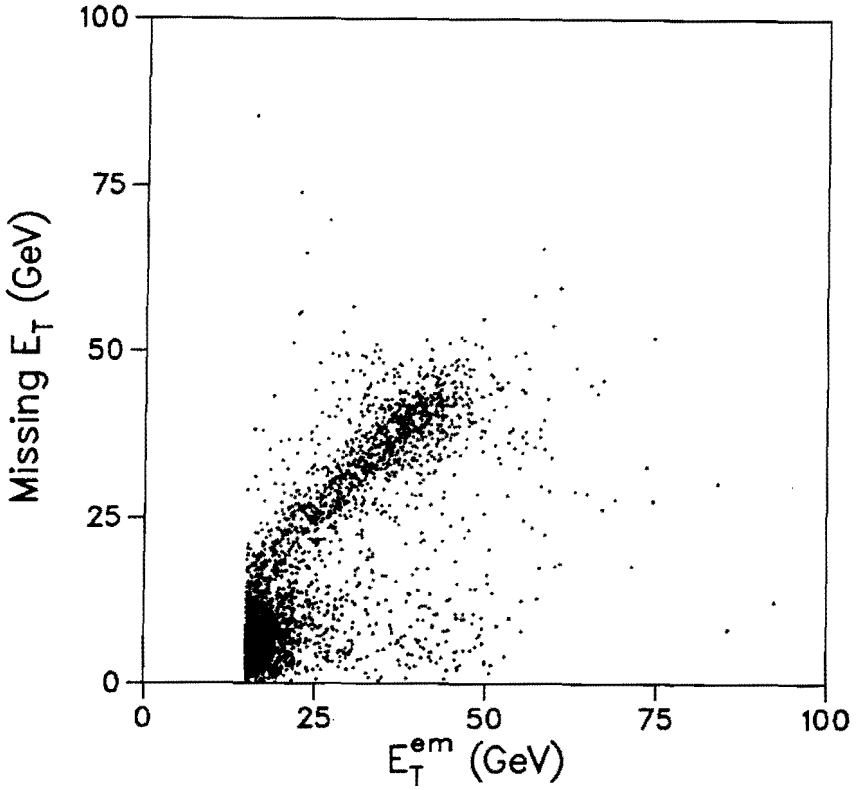

Figure 3.3: Scatterplot of $\not\!\!E_T$ vs E_T^{em} for the inclusive electron sample.

Z^0 candidates are explicitly removed by rejecting events with high-mass electron pairs, and the background from $W^{\pm}$ production is reduced by requiring several jets in the events. Finally, stricter cuts on E_T^{em} and $\not{E}_T$ are imposed to further reduce the backgrounds from b and c quark production and fake electrons to negligible levels.

3.2.1 Isolation

A majority of the electron candidates in the inclusive electron sample have E_T^{em} and $\not{E}_T$ less than 20 GeV (see Fig. 3.3). We have compared the inclusive electron data with the sample of Monte Carlo b and c quark events (see Sec. 2.4 for a description of the Monte Carlo sample). For this comparison $W^{\pm}$ bosons have been removed from the inclusive electron data by requiring the transverse mass ($M_T^{e\nu} \equiv \sqrt{2\, E_T^{em}\, \not{E}_T\, (1 - \cos\Delta\phi_{e\nu})}$, where $\Delta\phi_{e\nu}$ is the azimuthal difference between the electron and $\not{E}_T$ vectors) to be less than 40 GeV/c^2. The rate of observed events with $E_T^{em} < 20\ GeV$ is consistent with the ISAJET Monte Carlo prediction for these processes. Distributions such as the electron and leading and non-leading jet E_T spectra show good agreement with the Monte Carlo prediction (see Fig. 3.4). We have studied the jet spectra as a function of electron E_T, and have found agreement in the average jet E_T between data and Monte Carlo to better than 1.5 GeV over the range $12 < E_T^{em} < 20$ GeV.

Furthermore, the energy flow around the electron is well modeled by the Monte

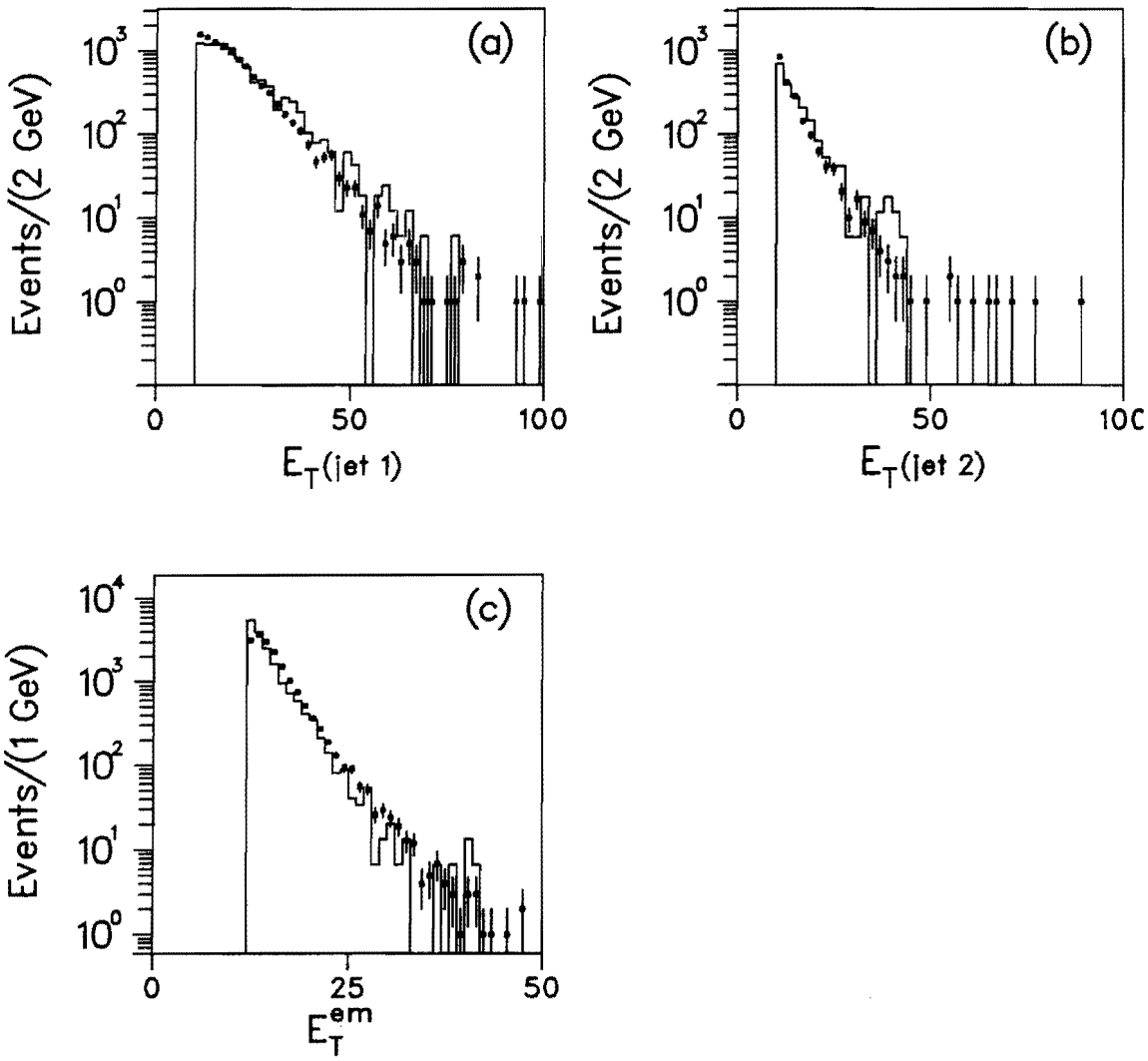

Figure 3.4: The E_T distributions for the leading and non-leading jets ((a) and (b)) and for the electron candidates (c) are shown as the plotted points. The histograms are the Monte Carlo predictions for b and c quark production.

Carlo. The isolation of an electron can be quantified by E_T^{iso}, defined as the sum of the transverse energy in calorimeter towers immediately adjacent to the electron cluster. Figure 3.5 shows the distribution of E_T^{iso} for electrons with $E_T^{em} < 20$ GeV along with the ISAJET prediction for b and c quark production. Also shown is the expected distribution for electrons from t quark decay, which are seen to be significantly more isolated. Because some residual W events are expected in the data at low E_T^{iso}, the Monte Carlo curve has been normalized to the data in the region above 0.5 GeV, and the $t\bar{t}$ curve has arbitrary normalization. We impose the cut

$$E_T^{iso} < 2\ GeV \tag{3.20}$$

to reduce these backgrounds to a possible top signal. The efficiency of this criterion for top quark events varies from 86–90% for M_{top} in the range 40–80 GeV/c^2. We estimate that it removes about 55% of the b and c quark events. There are $\sim$ 7 500 events that survive the isolation requirement.

3.2.2 Z^0 removal

Events containing a Z^0 boson decaying to an e^+e^- pair give rise to high-p_T electrons, which may contribute to the background in the top sample. Such events are removed by considering the invariant mass formed by the electron candidate with all other electromagnetic clusters in the event. Figure 3.6 shows this distribution for the inclusive isolated electron sample. Events which contain a pair with mass greater than

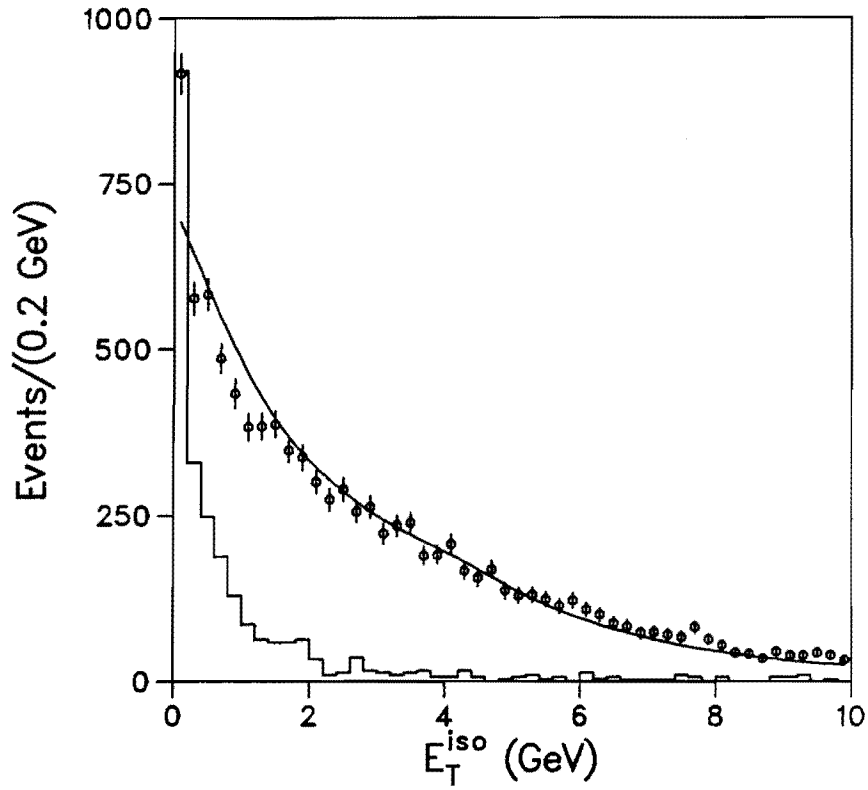

Figure 3.5: Isolation variable E_T^{iso} for electrons with $E_T^{em} < 20\ GeV$, for data (plotted points), $b\bar{b}$ Monte Carlo (solid curve), and $t\bar{t}$ ($M_{top} = 75$ GeV/c^2, histogram). The normalization of the Monte Carlo curves is discussed in the text.

70 GeV/c^2 are rejected. This cut effectively removes all Z^0 events in the sample, and the Monte Carlo efficiency for top events is greater than 99% for $M_{top} = 40$ GeV/c^2 and 96% for $M_{top} = 80$ GeV/c^2.

3.2.3 Jets

Four quark jets are expected in a $t\bar{t}$ event when one of the t quarks decays semileptonically. Conversely, most W's are produced without associated jet activity. Requiring the presence of several jets in the event significantly reduces the background from $W^{\pm}$ and Z^0 boson decays and (to a lesser extent) from b and c quark decay. We discuss here the jet cluster algorithm used to form jet clusters, jet energy scales and detection efficiency, and finally the jet cuts applied to the isolated electron sample.

Jet Clustering

Jets are detected as clusters of energy in the calorimeter, using a fixed-cone clustering algorithm. Preclusters are defined as contiguous sets of adjacent towers with $E_T > 1$ GeV. Clusters are formed from preclusters by considering all the towers within a cone in η-ϕ space of radius 0.7 centered on the precluster. All towers with $E_T > 0.1\ GeV$ within the cone are included in the cluster. The centroid of the cluster, defined as the E_T-weighted average, is calculated and the cone is repositioned on the centroid. Again, towers within the new cone passing the E_T cut are included in the cluster. This procedure is repeated until the towers in the cluster do not change.

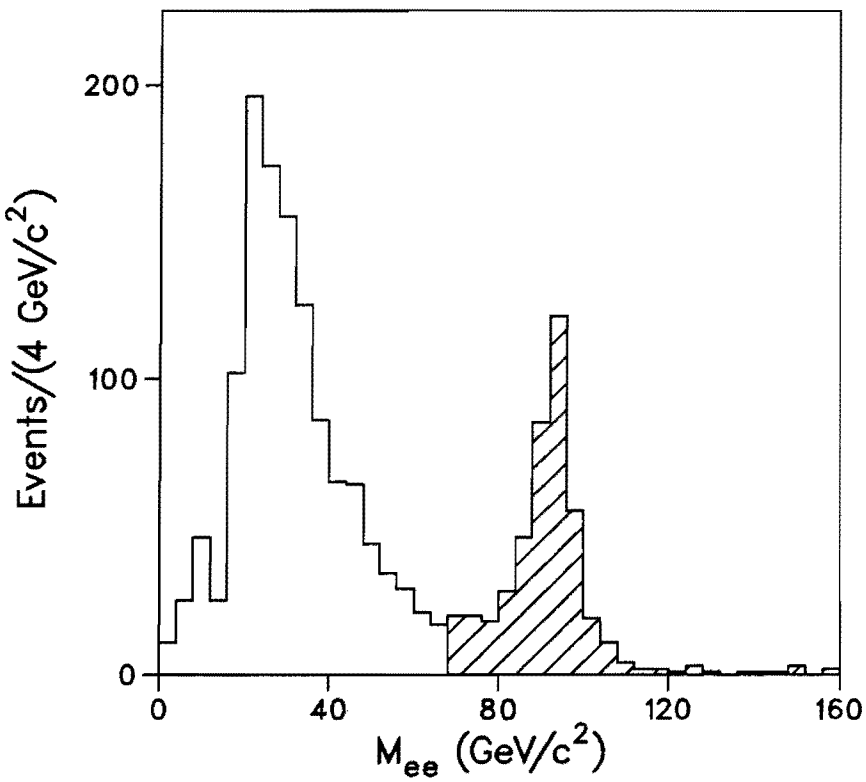

Figure 3.6: Mass spectrum of di-electron candidates. The shaded region is cut.

If a cluster is completely contained in a larger cluster, the smaller one is dropped. Partially overlapping clusters may be merged together, depending on the overlap fraction, defined as the E_T in the overlap region divided by the E_T in the smaller cluster. If the fraction is above 0.75, the two clusters are combined. Otherwise, the towers in the overlap region are divided between the two clusters according to their proximity to the cluster centroid. After this division, the centroids are re-calculated and the towers in the original overlap region are re-divided based on their distance from the new centroids. This procedure is iterated until a stable configuration is reached.

Jet Energy Scale and Detection Efficiency

The following procedure was used to model the response of the detector to jets. The central calorimeter simulation was tuned on CDF test beam data, using pions with momenta between 15 and 150 GeV/c, and electrons with momenta between 10 and 50 GeV/c. The simulation was adjusted to give the correct response in both the "face" and "crack" regions of the calorimeter, where the "crack" region is defined as within 2° of a central wedge boundary. The response to lower energy pions (0.5 to 10 GeV) was determined *in situ* by considering isolated charged tracks in minimum bias events. In this case, the calorimeter response was determined using the transverse momentum as reconstructed in the central tracking chamber. A subtraction for neutral energy

accompanying the track was performed in this study. The systematic uncertainty in the jet energy scale has been estimated for central jets with observed transverse energy between about 18 and 180 GeV, with the error ranging from 13% for the lower energy jets to 5% for the higher energy jets.

We verified the jet energy scale by considering direct photon production, which is dominated by a high-p_T photon recoiling against a single parton. Direct photon events are selected by requiring an electromagnetic shower in the central calorimeter without a track pointing to it. Photons from π^0 decay are rejected by requiring a high quality shower profile in the central strip chambers. The photon was required to be isolated, with no other clusters with $E_T > 3$ GeV in the same hemisphere. In these events, the transverse momentum of the photon balances the p_T of the recoil parton. Thus, a comparison between the photon E_T and the E_T of the leading jet in the opposite hemisphere allows one to determine the efficiency for detecting jets above some E_T threshold as a function of parton p_T. A comparison between the direct photon data and an ISAJET calculation shows the jet energy scale in the simulation to agree with the data. Figure 3.7 shows the probability for finding a jet cluster with $E_T > 10$ GeV in the hemisphere opposite the photon as a function of the parton transverse momentum. The Monte Carlo prediction is shown as the solid curve; the agreement is very good within the statistics.

Further confidence in the jet energy scale comes from the comparison of jet E_T

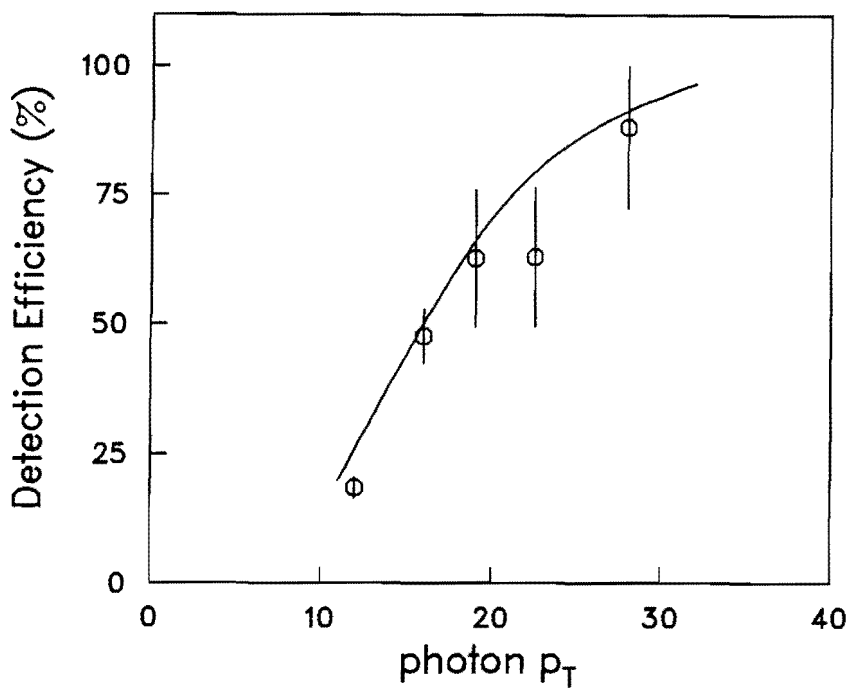

Figure 3.7: Probability of finding a jet cluster with $E_T > 10$ GeV in the hemisphere opposite the photon for direct photon events. The horizontal axis is the photon p_T (assumed equal to the parton p_T). The solid curve is the Monte Carlo prediction.

Table 3.5: Summary of jet cuts.

Variable	Cut
n_{jets}	≥ 2
$E_T^{jet_1}$	> 10 GeV
$E_T^{jet_2}$	> 10 GeV
$\lvert\eta_{jet}\rvert$	< 2

spectra in the inclusive electron sample with the Monte Carlo calculation for b and c production, as discussed above (see Sec. 3.2.1). Based on these studies we conservatively estimate the systematic uncertainty in the Monte Carlo jet energy scale to be less than 20% for a jet with an E_T of 10 GeV.

Jet Selection Criteria

We require events for the electron + jets sample to have two or more jets with each jet required to have at least 10 GeV of observed energy. Furthermore, because the pseudorapidity distribution of jets from $t\bar{t}$ production is significantly narrower than that from $W^{\pm}$ or b quark production (see Fig. 3.8), the jets are required to have $|\eta_{jet}| < 2$, where the pseudorapidity of the jets is measured relative to the center of the detector. A summary of the jet cuts is shown in Table 3.5.

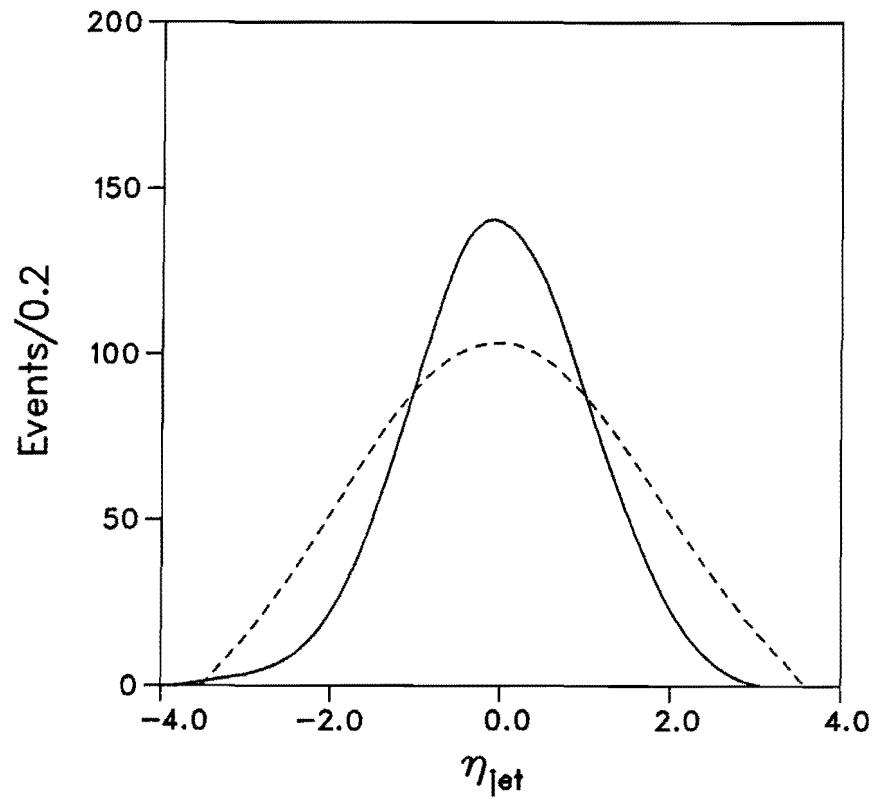

Figure 3.8: Monte Carlo distributions of the pseudorapidity of jets from top (M_{top} = 75 GeV/c^2, solid curve) and W + 2 jet events (dashed curve).

3.3 Kinematic cuts - final sample

Electrons and neutrinos from top quark decay typically have transverse energies greater than 15 GeV. We therefore make tighter cuts on E_T^{em} and $\not{E}_T$ to define our final event sample. We then discuss the backgrounds to top in the final sample.

3.3.1 "Loose" and "Tight" E_T and $\not{E}_T$ cuts

The scatterplot of $\not{E}_T$ vs E_T^{em} for the 922 events in the electron + 2 jet sample is shown in Fig. 3.9(a) (we use "electron + 2 jets" to signify an event with an electron plus two or more jets). Also shown is the expected $\not{E}_T$ vs E_T^{em} plot for $t\bar{t}$ production for a top mass of 70 GeV and for W + 2 jet production (Figs. 3.9(b) and (c), respectively). These scatterplots (and all scatterplots of Monte Carlo data in the report) have not been normalized to the data; their equivalent integrated luminosities are given in Sec. 2.4. In the region of high E_T^{em} and $\not{E}_T$ the data resemble W events. Also, there are a large number of events in the data, clustered at low E_T^{em} and $\not{E}_T$, that cannot be interpreted as resulting from top or W production. We present in Fig. 3.10(a) the distribution of $\not{E}_T$ vs E_T^{em} for events identified as conversion candidates, a sample which has characteristics similar to the QCD background present in the data. Figure 3.10(b) shows the same distribution for non-isolated electron + 2 jet events ($E_T^{iso} > 2$ GeV), a sample enriched in events from b quark production. Both samples of events cluster at low values of $\not{E}_T$ and E_T^{em}. To further reduce

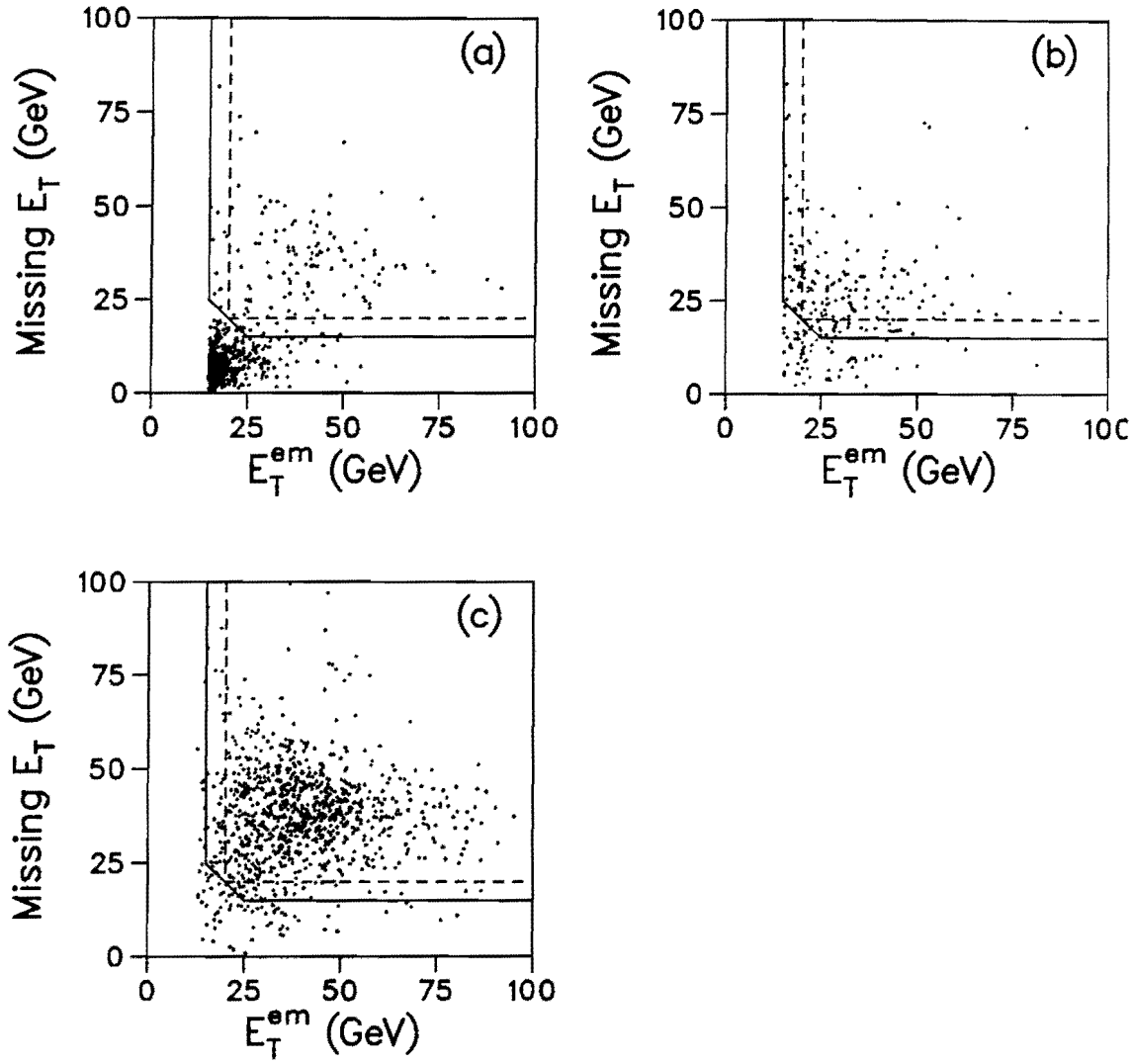

Figure 3.9: Scatterplot of $\not\!\!E_T$ vs E_T^{em} for events with an electron and two or more jets. Conversions and Z^0 events have been removed as described in the text. (a) data, with the contours for the tight and loose kinematic cuts, (b) Monte Carlo $t\bar{t}$ with $M_{top} = 70$ GeV/c^2, (c) Monte Carlo W + 2 jet events.

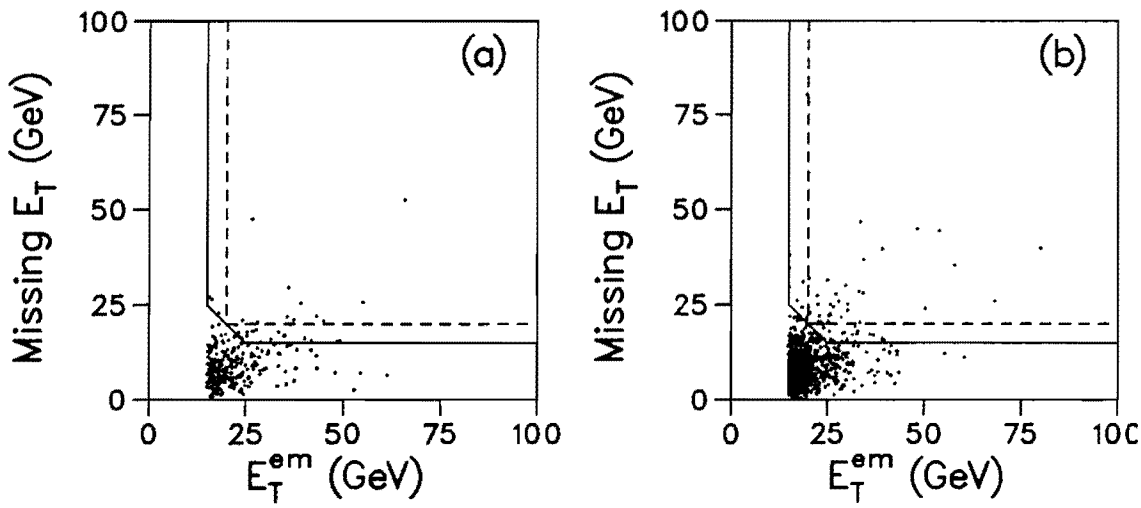

Figure 3.10: $\not\!\!E_T$ vs E_T^{em} scatterplot for background events. (a) conversion events, and (b) non-isolated electrons ($E_T^{iso} > 2$ GeV).

the backgrounds from b and c quark production and QCD processes, the following kinematic cuts are made on E_T^{em} and $\not{E}_T$, (hereafter referred to as "loose" cuts):

$$\begin{aligned} E_T^{em} &> 15 \text{ GeV}, \\ \not{E}_T &> 15 \text{ GeV}, \\ E_T^{em} + \not{E}_T &> 40 \text{ GeV}. \end{aligned} \tag{3.21}$$

There are 123 electron + 2 jet events that survive the loose kinematic cuts. When making comparisons to the predictions for higher top masses stricter kinematic cuts will be applied (referred to as "tight" cuts):

$$\begin{aligned} E_T^{em} &> 20 \text{ GeV}, \\ \not{E}_T &> 20 \text{ GeV}, \end{aligned} \tag{3.22}$$

There are 104 events that pass the tight cuts. The efficiencies of these kinematic cuts for t quark events have been determined from Monte Carlo data and are shown in Table 3.6 for various top masses. The contours of these two sets of kinematic cuts are shown in Fig. 3.9.

3.3.2 Backgrounds in the final sample

We estimate the background due to b and c quark production and QCD fake electrons in our final sample by considering the effect of the isolation (E_T^{iso}) cut. The method is similar to that applied to the case of the charged pion background in the inclusive

Table 3.6: Efficiency of kinematic cuts as a function of M_{top}.

M_{top} (GeV/c^2)	"Loose" Cuts	"Tight" Cuts
40	0.25 ± 0.02	0.13 ± 0.02
50	0.49 ± 0.03	0.25 ± 0.03
60	0.63 ± 0.03	0.37 ± 0.03
70	0.73 ± 0.03	0.47 ± 0.03
75	0.75 ± 0.02	0.55 ± 0.02
80	0.79 ± 0.02	0.59 ± 0.03

electron sample where the *had/em* distribution was used to estimate the size of that background (see Sec. 3.1.3). We assume that all the electrons in the sample result either from W decays or from the sources of non-isolated electrons previously mentioned; since the isolation of electrons from t quark decays is similar to that from $W^{\pm}$ decays, this approximation is valid even if there is a significant amount of top in the sample. Equations (3.15) and (3.16) can be used with the substitutions $e \leftrightarrow W$ and $\pi \leftrightarrow b$. Now ϵ_W and ϵ_b are the efficiencies of the E_T^{iso} cut for electrons from $W^{\pm}$ decay and non-isolated sources, respectively. The efficiency of the E_T^{iso} cut for W + jet events is found to be $\epsilon_W = .93 \pm .02$ from studies of Monte Carlo data and of a sample of W events that have very high missing E_T and satisfy loose electron selection.

Table 3.7: Summary of numbers used to calculate the non-isolated electron background in the electron + 2 jet sample.

		"Loose" Cuts	"Tight" Cuts
efficiency of E_T^{iso} cut for $W^{\pm}$ + jets	ϵ_W	$0.93 \pm .02$	
efficiency of E_T^{iso} cut for non-isolated background	ϵ_b	$0.33 \pm .05$	
electron + 2 jet candidates	N_p	123	104
events failing E_T^{iso} cut only	N_f	65	33
number of real $W^{\pm}$'s	N_W	102 ± 33	98 ± 28
number of real non-isolated electrons	N_b	86 ± 30	39 ± 26
BG as % of sample	f_{bg}^{non}	$23 \pm 9\%$	$12 \pm 8\%$

The efficiency for non-isolated electron candidates is found to be $\epsilon_b = .33 \pm .05$ from studies of E_T^{iso} for events with low $\not{E}_T$, conversion electron candidates, and candidates passing all the electron selection criteria except the *had/em* cut. N_W and N_b are the calculated numbers of real $W^{\pm}$'s and non-isolated electrons in the sample, before applying the E_T^{iso} cut. The results are shown in Table 3.7.

We estimate the background due to conversions and charged pions in the final

Table 3.8: Conversion efficiency and background as a function of electron E_T.

	$E_T^{em} > 12\ GeV$	$E_T^{em} > 15\ GeV$	$E_T^{em} > 20\ GeV$
ϵ_{conv}	$.868 \pm .021$	$.885 \pm .029$	$.903 \pm .050$
f_{prompt}	$.113 \pm .002$	$.101 \pm .002$	$.065 \pm .003$
f_{bg}	$.051 \pm .008$	$.044 \pm .013$	$.026 \pm .013$

sample using the same techniques described in Sec. 3.1.3. The conversion detection efficiency varies with electron E_T and is shown in Table 3.8. Also shown is the amount of background remaining in a sample with a given E_T^{em} threshold. The "loose" and "tight" kinematic cuts correspond to E_T^{em} of 15 GeV and 20 GeV, respectively. For the charged pion background in the final sample, we consider the number of events that pass all the final cuts except the *had/em* cut. For the loose cuts we find the number failing, $N_f = 6$, which gives a background fraction of $0.0 \pm 3.2\%$. Four events fail the the *had/em* using the tight cuts, giving a background fraction of $0.0 \pm 4.8\%$. These non-electron background estimates for the final sample are summarized in Table 3.9. We attribute the difference between the non-isolated electron background estimate and the background estimate for conversions plus $\pi^{\pm}$ to b and c quark production.

Table 3.9: Summary of non-electron background for final sample of electron + 2 jet events.

	"Loose" Cuts	"Tight" Cuts
$\pi^{\pm}$	$0 \pm 3\%$	$0 \pm 5\%$
$\gamma \to e^+e^-$	$4.4 \pm 1.3\%$	$2.6 \pm 1.3\%$
Total	$4.4 \pm 3\%$	$2.6 \pm 5\%$

W + jets

Based on the distribution of E_T and $\not{E}_T$, the electron + 2 jet data appears to be composed primarily of W + 2 jet events. In this section we present comparisons of the data and the W + 2 jet Monte Carlo sample for several other characteristic variables. In what follows we interpret the missing E_T as the p_T of an undetected neutrino. The transverse momentum of the (real or virtual) W boson ($p_T^{e\nu}$) is the vector sum of E_T^{em} and $\not{E}_T$:

$$p_T^{e\nu} = \left|\vec{E}_T^{em} + \vec{\not{E}}_T\right|. \tag{3.23}$$

The scatterplot of $M_T^{e\nu}$ vs $p_T^{e\nu}$ for the electron + 2 jet sample with loose cuts is shown in Fig. 3.11(a), along with the corresponding distribution for W + 2 jet events (Fig. 3.11(b)). The "hole" in the distribution in the lower left corner is caused by the loose kinematic cuts. There is good agreement between data and Monte Carlo. The projections of these variables are shown in Fig. 3.12, where the agreement be-

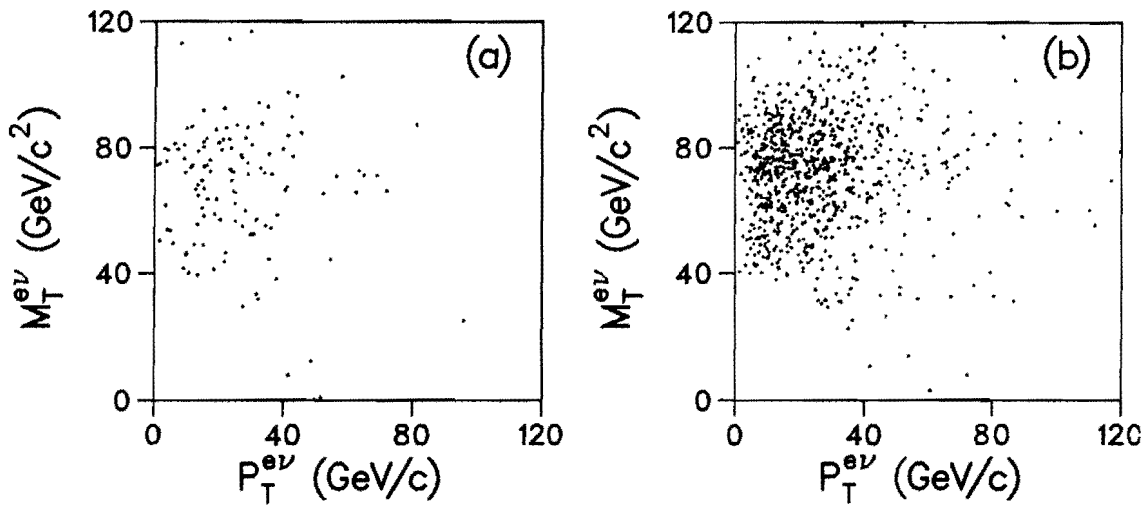

Figure 3.11: Scatterplot of $M_T^{e\nu}$ vs $p_T^{e\nu}$ for the electron + 2 jet data sample with the loose cuts. (a) electron + 2 jet data, (b) W + 2 jet Monte Carlo.

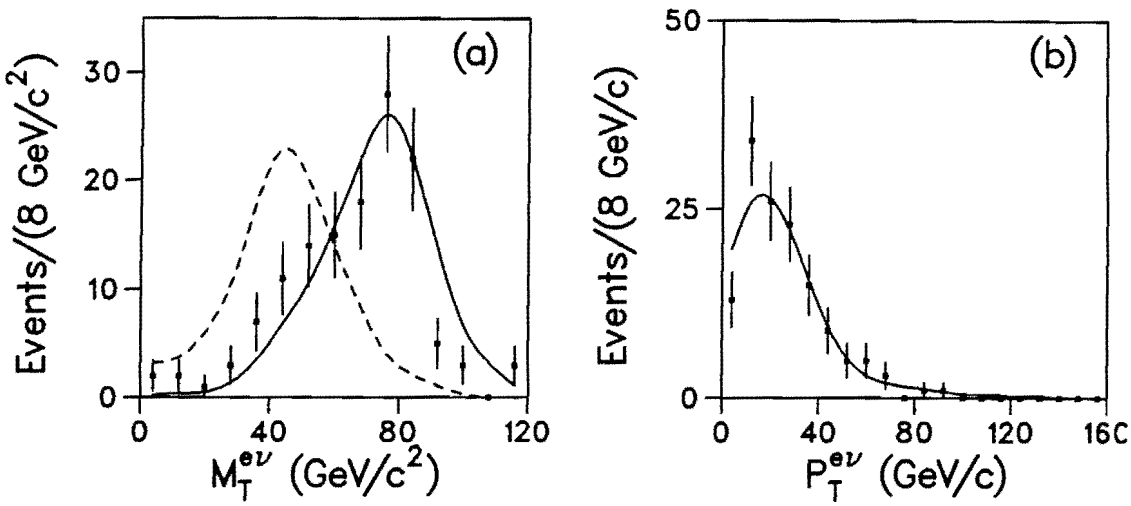

Figure 3.12: $M_T^{e\nu}$ and $p_T^{e\nu}$ for electron + 2 jet data, with the loose cuts applied. (a) $M_T^{e\nu}$ for data events, Monte Carlo W + 2 jet events (solid curve, normalized to the data), and Monte Carlo $t\bar{t}$ events for $M_{top} = 60$ GeV/c^2 (dashed curve, normalized to the number of events predicted by the Altarelli cross section), (b) $p_T^{e\nu}$ for data events and W + 2 jet Monte Carlo events (solid curve).

tween data and Monte Carlo is even more apparent. Figures 3.13(a)-(c) show the invariant mass of the two highest E_T jets (M_{jj}), the azimuthal difference between these jets ($\Delta\phi_{jj}$), and the difference in pseudorapidity between them ($\Delta\eta_{jj}$), respectively. There is good agreement with the W + 2 jets Monte Carlo prediction. Other distributions including the jet E_T spectra and the angle between electron and jets also show good agreement with the W + 2 jet Monte Carlo calculation. This good agreement indicates that the final sample is composed primarily of W + jet events.

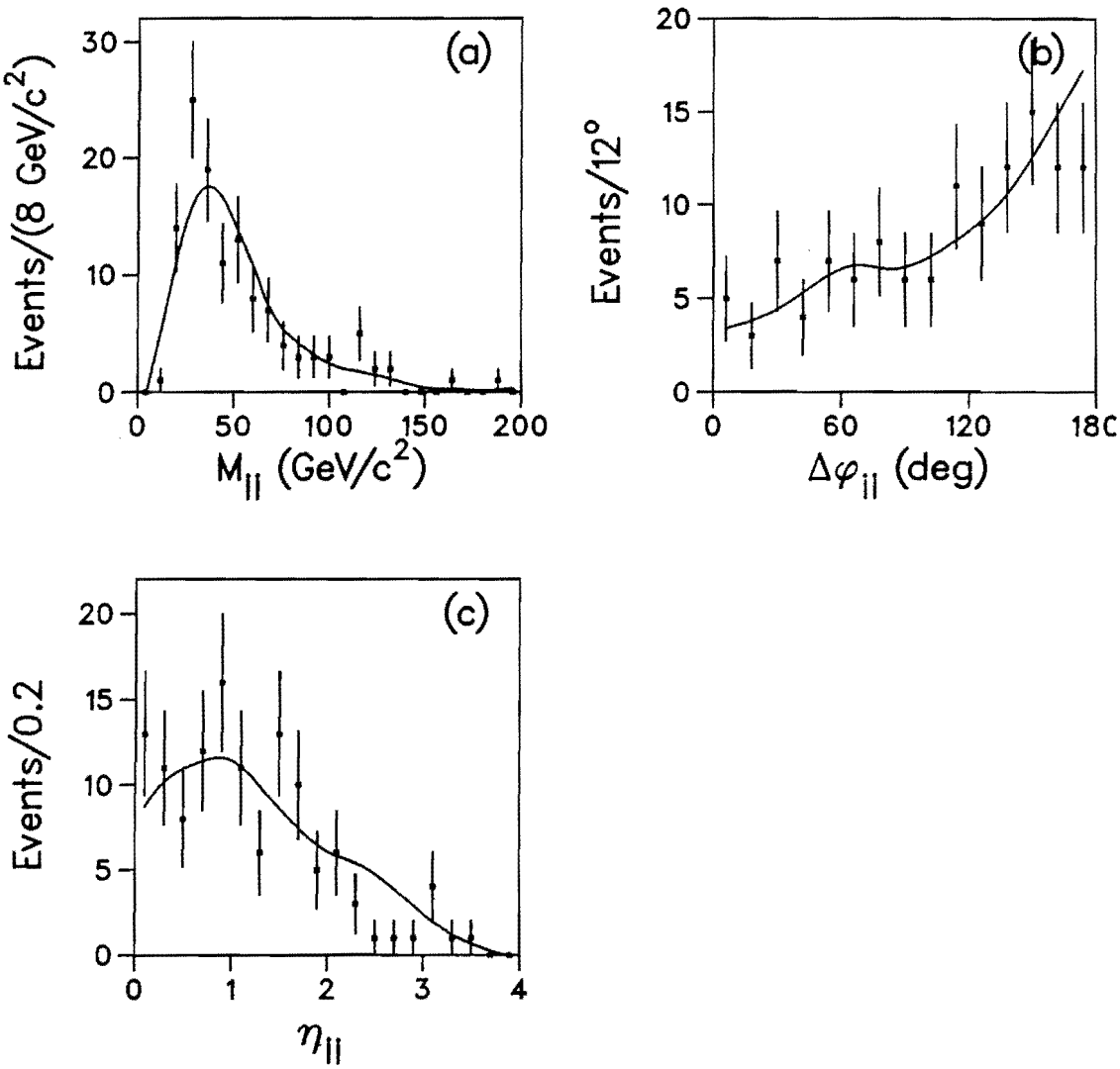

Figure 3.13: Comparison of the electron + 2 jet data with the loose cuts applied (plotted points) with the W + 2 jet Monte Carlo predictions (solid curves): (a) di-jet invariant mass, (b) azimuthal difference between the two leading jets, and (c) pseudorapidity difference between the two leading jets.

To place an upper limit on the fraction of observed events that can be attributed to top quark production, we will compare the observed transverse mass distribution to that expected from W boson and top quark production.

Chapter 4

Transverse Mass Analysis

4.1 Transverse mass

The transverse mass is a quantity well suited for distinguishing between W + jet production and t quark production, if the top quark mass is below the threshold for the decay $t \rightarrow Wb$, where the W in the final state is real (as opposed to virtual) [20]. In particular, if the top mass is below the mass of the W, the distribution of $M_T^{e\nu}$ will be significantly softer for top events than for W events (see Fig. 4.1). We place an upper limit on the rate of top quark production by comparing the shapes of the transverse mass distributions measured in the electron + 2 jet data with those expected from top and W + jet production.

4.1.1 Measuring and modeling transverse mass

We have verified our ability to measure and model the transverse mass in electron + 2 jet events by studying inclusive electron events, Z^0 events, and the electron + 1 jet

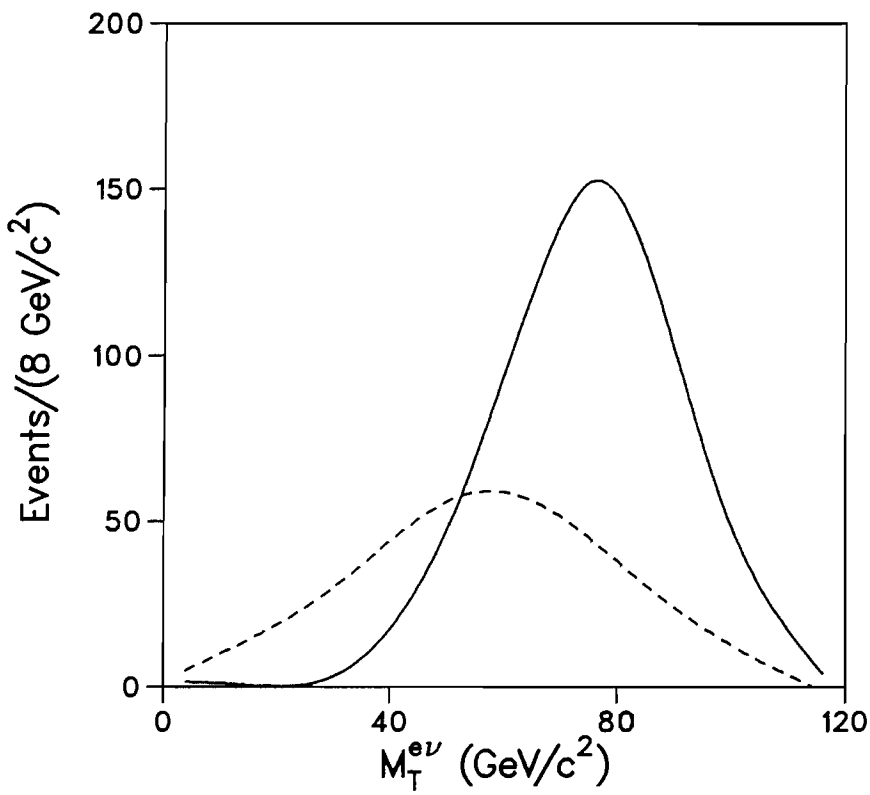

Figure 4.1: Monte Carlo distributions of $M_T^{e\nu}$ for top quarks with $M_{top} = 75$ GeV/c^2 (solid curve) and W + 2 jet events (dashed curve).

sample. Events with an electron and exactly one jet (with $E_T^{jet} > 10\ GeV$) provide a good testing ground for transverse mass measurements. Whereas the electron + 2 jet sample is possibly a mixture of $W^{\pm}$ and top events, it is expected that the electron + 1 jet events are dominated by W + 1 jet production (the maximum contribution from top quark events is less than 15%, which occurs for $M_{top} \sim 60$ GeV/c^2). The jet requirement implies that there is significant hadronic energy in these events, so that the $\not{E}_T$ resolution is similar to that in the electron + 2 jet sample.

A potential problem in the electron + 1 jet sample is the amount of background from dijet events, where one jet fakes an electron. To reduce this background, we impose a strict isolation cut, requiring

$$I = \frac{E_T^{cone} - E_T^{em}}{E_T^{cone}} < 0.1, \tag{4.1}$$

where E_T^{cone} is the transverse energy in a cone with radius $\Delta R = 0.7$ about the electron. To further reduce the background from dijet events an explicit cut on the presence of a jet opposite the electron is made. Specifically, the event is rejected if there is a jet present such that

$$E_T^{jet} > 5 \text{ GeV/c}^2 \quad \text{and} \quad 165^\circ < \Delta\phi_{ej} < 195^\circ, \tag{4.2}$$

where $\Delta\phi_{ej}$ is the azimuthal angle between the electron and jet vectors. The transverse mass distribution of events passing the tight kinematic cuts (see Sec. 3.3.1) is shown in Fig. 4.2(a), along with the W + 1 jet distribution from the PAPAGENO Monte

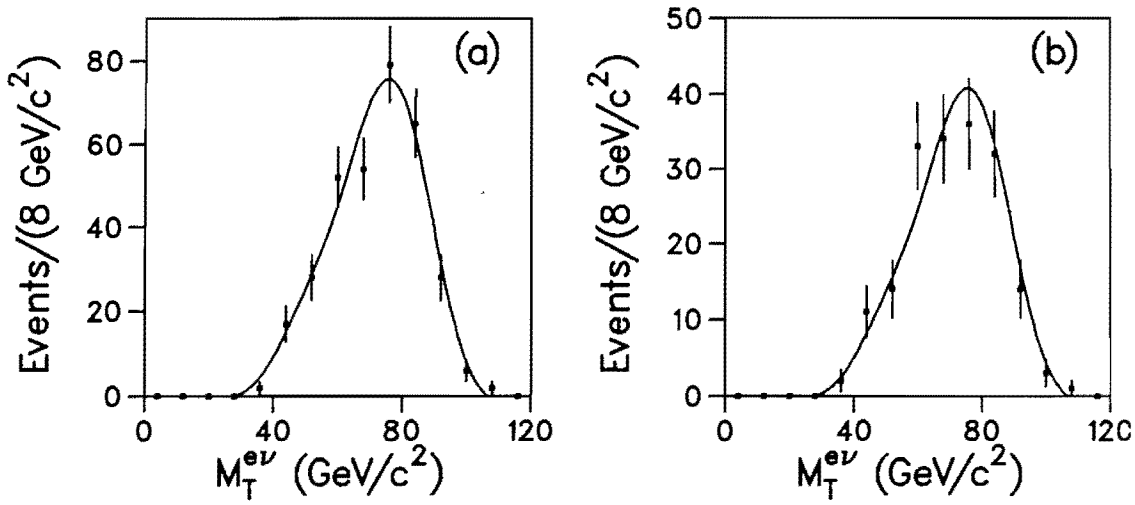

Figure 4.2: Transverse mass for electron + 1 jet events with the tight cuts applied. (a) full electron + 1 jet sample, (b) subset of electron + 1 jet events where more $M_T^{e\nu}$ smearing is expected as described in the text.

Carlo calculation employing the full detector simulation. The agreement between the electron + 1 jet data and the W + 1 jet calculation is excellent.

To further test the measurement of $M_T^{e\nu}$, we select a subset of the electron + 1 jet events, in which the Monte Carlo calculation predicts more smearing in $\not{E}_T$. We select events that satisfy any of the following:

$$E_T^{jet} > 20\ GeV$$

$$15^\circ < \Delta\phi_{ej} < 60^\circ \tag{4.3}$$

$$120^\circ < \Delta\phi_{ej} < 165^\circ.$$

The Monte Carlo calculation indicates that the transverse mass resolution for these events is within 15% of the $M_T^{e\nu}$ resolution for W + 2 jet events. The transverse mass of this subset of the electron + 1 jet sample is shown in Fig. 4.2(b). Again the agreement between data and Monte Carlo is very good, and we conclude that the transverse mass in the electron + 2 jet sample is well modeled by the detector simulation.

4.1.2 Fitting transverse mass

We determine an upper limit on the production of $t\bar{t}$ pairs by fitting the transverse mass distribution of the electron + 2 jet sample to the theoretically predicted distributions for top quarks and for $W^\pm$ bosons. We assume that the electron + 2 jet data sample contains only $W^\pm$ and top events so that the $M_T^{e\nu}$ distribution of the observed events is given by

$$\frac{dN}{dM_T^{e\nu}} = \alpha T(M_T^{e\nu}) + \beta W(M_T^{e\nu}) \tag{4.4}$$

where $T(M_T^{e\nu})$ and $W(M_T^{e\nu})$ are the theoretical $M_T^{e\nu}$ distributions for $W^\pm$ and top, respectively, and the coefficients α and β are determined by the fit. The function $T(M_T^{e\nu})$ varies as a function of top mass and the fitting procedure is performed for each

top mass investigated. As discussed previously, the ISAJET and PAPAGENO Monte Carlo programs plus the full detector simulation were used to determine the functions $T(M_T^{e\nu})$ and $W(M_T^{e\nu})$. For fitting purposes these functions have been normalized to the integrated luminosity of the real data (4.4 pb^{-1}). This way the coefficients α and β can be easily interpreted as the fraction of the predicted amount of top and $W^{\pm}$ in the data. Specifically, if top quarks and W bosons were present in the data with the rates predicted by the theoretical calculations, α and β will both be equal to one. We emphasize that we are not relying on the predicted rate of $W^{\pm}$ + 2 jet events, but only on the shape of the $M_T^{e\nu}$ distribution of these events. We discuss below the consequences of ignoring contributions other than top quark and $W^{\pm}$ events to the electron + 2 jet sample.

Effect of other backgrounds

As discussed previously, the electron + 2 jet sample contains known contributions from sources other than W + jet production. Besides backgrounds from b and c quark production and QCD sources, W production with $W \rightarrow \tau\nu_\tau \rightarrow e\nu_e\nu_\tau\nu_\tau$ is expected to contribute. We have not attempted to model these contributions to the $M_T^{e\nu}$ distribution. In addition, if $M_{top} \lesssim 65$ GeV/c^2, there will be some contribution of t quarks from the decay $W \rightarrow t\bar{b}$. Because the rate for this process is low relative to the $t\bar{t}$ rate, we neglect this source of top quarks. Since all of these sources produce

events at low values of transverse mass, the fitted fraction of $t\bar{t}$ events will tend to increase. Thus this method results in a conservative estimate of the fraction of events attributed to $t\bar{t}$ production.

Fitting method

The fit used is a binned maximum likelihood method, with the contents of the bins treated with Poisson statistics. Let k_i be the number of events observed in the ith $M_T^{e\nu}$ bin and let m_i be the number of predicted events in the bin. The probability associated with the ith bin is

$$P_i(k_i, m_i) = \frac{m_i^{k_i} e^{-m_i}}{k_i!}. \tag{4.5}$$

The total probability is then the product of the individual probabilities for each bin

$$\begin{aligned} P &= \prod_{i=1}^{N} P_i(k_i, m_i) \\ &= \prod_{i=1}^{N} \left(\frac{m_i^{k_i}}{k_i!} \right) e^{-\sum m_i}, \end{aligned} \tag{4.6}$$

where N is the total number of bins in the fit. It is more convenient to maximize the logarithm of the likelihood,

$$\ln P = \sum_i \left(-\ln k_i! + k_i \ln m_i - m_i \right). \tag{4.7}$$

The dependence on α and β in Eq. (4.7) is contained in the m_i. We therefore may ignore the first term in this equation for the purposes of maximizing $\ln P$ with respect

to α and β. The quantity maximized by the fitting routine is then given by

$$\ln P = \sum_i (k_i \ln m_i - m_i) . \tag{4.8}$$

The program MINUIT [21] was used to maximize this expression.

We fit the transverse mass distributed in 8 GeV/c^2 bins over the range 24–120 GeV/c^2. We exclude the lowest bins of transverse mass to help minimize the non-W backgrounds discussed above. Few top or W events are expected with very low transverse mass values, especially once the kinematic cuts have been applied. Additionally, the coefficients α and β are constrained to be greater than zero on physical grounds, using the procedure described in reference [22].

Fit results

The results of the fits are presented in Table 4.1. The fits are in good agreement with the data. The binned χ^2 is shown as an indication of the quality of fit. The statistical errors shown correspond to a change in the log-likelihood of 1/2 unit. Contour plots of α vs β are shown in Fig. 4.3 for two values of top mass. The small fitted values of α indicate an absence of top in the data, while the values of β obtained are within the theoretical uncertainties of the predicted W + jet cross sections, which are estimated to be 30–50% [23].

To translate these fit values into a limit on the top mass, one must take into account systematic errors.

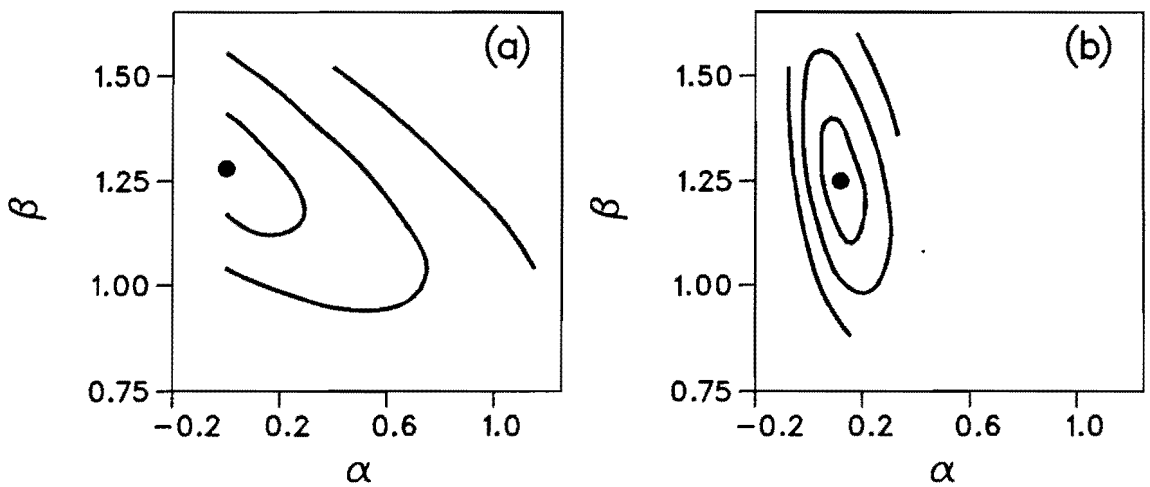

Figure 4.3: Fit contours in α, β space, as calculated by MINUIT: (a) M_{top} = 80 GeV/c^2, (b) M_{top} = 60 GeV/c^2. The contours correspond to changes in the log-likelihood function of 0.5, 2.0, and 4.5. The constraint $\alpha > 0$ has been imposed for the 80 GeV/c^2 fit.

Table 4.1: Transverse mass fit results. The loose cuts were used for $40 \leq M_{top} < 65$ GeV/c^2 and the tight cuts were used for the other top masses. The uncertainties shown are statistical.

M_{top} GeV/c^2	α	β	χ^2 (10 dof)
40	0.07 ± 0.05	1.27 ± 0.14	9.7
50	0.06 ± 0.05	1.29 ± 0.14	10.4
60	0.11 ± 0.08	1.26 ± 0.15	10.4
70	$0.00^{+0.12}_{-0.00}$	1.28 ± 0.13	9.4
75	$0.00^{+0.18}_{-0.00}$	1.28 ± 0.13	9.4
80	$0.00^{+0.27}_{-0.00}$	1.28 ± 0.13	9.4

4.2 Systematic uncertainties

We divide the systematic uncertainties into two groups. The first group consists of those effects that can affect both the shape of the $M_T^{e\nu}$ distribution as well as the number of events accepted. An investigation of the effect of these uncertainties on the top mass limit requires refitting the $M_T^{e\nu}$ distribution for each variation of the uncertain quantity. The systematic uncertainty associated with these effects is denoted $\Delta\alpha$. The second group of systematic uncertainties contains those effects that have been determined to affect only the rate of accepted events and not the shape of the $M_T^{e\nu}$ distributions. These effects contribute to an uncertainty in the overall

normalization. The systematic error due to these effects is expressed fractionally and is denoted Δn.

4.2.1 Systematic uncertainties in determining α

The uncertainties for which refitting of the $M_T^{e\nu}$ distribution is necessary are

- the uncertainty in the jet energy scale in the Monte Carlo calculation,
- the uncertainty in the model of the underlying event, and
- the $M_T^{e\nu}$ interval over which the fit is performed.

Other sources of uncertainty have been studied and found to be negligible.

The estimated uncertainty on the Monte Carlo jet energy scale is $\pm 20\%$ (see Sec. 3.2.3). The underlying event E_T is defined as the vector E_T of all energy that is not contained in either the electron cluster or in jet clusters with at least 5 GeV of observed transverse energy. A comparison of the underlying event E_T in electron + 2 jet events was made for real data, PAPAGENO W + 2 jet events, and ISAJET $t\bar{t}$ events. The mean E_T's of the underlying event agree to within 15% for the three samples; conservatively, we take the uncertainty in the underlying event E_T to be $\pm 20\%$.

We estimated the uncertainty in α by varying the scale (jet energy or underlying event energy) by the amounts stated above, recalculating the theoretical functions $T(M_T^{e\nu})$ and $W(M_T^{e\nu})$ and then refitting the $M_T^{e\nu}$ distributions. For example, if the

jet energy scale is being varied, all jets in the event are multiplied by the appropriate factor (e.g., 1.2). The $\not\!\!E_T$ is recalculated and the jet cuts and the kinematic cuts are applied using the new jet energies and $\not\!\!E_T$. The transverse mass is then recalculated for events passing the cuts. In this way, changes in both acceptance and transverse mass are taken into account when determining the new $M_T^{e\nu}$ distributions, $T(M_T^{e\nu})$ and $W(M_T^{e\nu})$.

Table 4.2 shows the values of α obtained by refitting the transverse mass after making the variations in scale described above. This table also shows the effect of the particular choice of $M_T^{e\nu}$ interval over which the fit is performed. This is estimated by refitting over the intervals 16–120 GeV/c^2 and 32–120 GeV/c^2. The nominal fit results are also provided for comparison.

An uncertainty in α is computed for each systematic effect at each value of M_{top} using the following guidelines. If the shifts in α for the positive and negative variations for a given effect are in opposite directions, half the range is taken as the uncertainty in α. If the shift in α is in the same direction for the positive and negative variations, then the average shift is taken as the uncertainty. The 70 and 80 GeV/c^2 cases show no shift in the best value of α. The fit would prefer a value of α less than zero (by about 1/2 standard deviation), but α is constrained by the fit to be greater than zero. For the 80 GeV/c^2 case we consider the shift in the statistical error to estimate the uncertainty (using the rules described above). For the 70 GeV/c^2 case we have also

Table 4.2: Systematic variation of fitted $t\bar{t}$ fraction α. The errors shown are statistical only. The loose cuts have been used for $M_{top} < 65$ GeV/c^2, the tight cuts for the other masses.

M_{top}	Nominal	Jet Energy		Underlying		Fit Interval	
(GeV/c^2)	Fit	Scale		Event		(GeV/c^2)	
		+20%	-20%	+20%	-20%	16–120	32–120
40	$.07 \pm .05$	$.05 \pm .04$	$.05 \pm .07$	$.07 \pm .05$	$.07 \pm .07$	$.03 \pm .05$	$.07 \pm .05$
50	$.06 \pm .05$	$.06 \pm .05$	$.07 \pm .07$	$.05 \pm .05$	$.04 \pm .05$	$.05 \pm .05$	$.05 \pm .05$
60	$.11 \pm .08$	$.07 \pm .06$	$.13 \pm .11$	$.10 \pm .09$	$.11 \pm .08$	$.06 \pm .07$	$.09 \pm .08$
70	$.00 \pm .12$	$.00 \pm .08$	$.00 \pm .13$	$.00 \pm .12$	$.00 \pm .11$	$.00 \pm .09$	$.00 \pm .17$
75	$.00 \pm .17$	$.00 \pm .21$	$.00 \pm .18$	$.00 \pm .17$	$.00 \pm .18$	$.00 \pm .12$	$.00 \pm .26$
80	$.00 \pm .27$	$.00 \pm .33$	$.00 \pm .46$	$.00 \pm .21$	$.00 \pm .30$	$.00 \pm .22$	$.00 \pm .45$

Table 4.3: Systematic variations in α for $M_{top} = 70$ GeV/c^2. The fit coefficients α, and β are allowed to go negative for this fit.

Systematic Effect	$t\bar{t}$ fraction, α
Nominal	$-0.06 \pm .14$
Jet Scale +20%	$-0.15 \pm .16$
Jet Scale −20%	$-0.16 \pm .18$
Underlying Event +20%	$-0.08 \pm .17$
Underlying Event −20%	$-0.11 \pm .18$

fit the data allowing α to be less than zero and considering the shift in the best value of α obtained. The results of that fit are shown in Table 4.3. The contributions to $\Delta\alpha$ from each of the three systematic effects discussed above are added in quadrature to form the results shown in Table 4.4. As discussed above, these values of $\Delta\alpha$ are derived only from the effects for which it was necessary to refit the $M_T^{e\nu}$ distribution. Additional systematic uncertainties in the overall normalization (Δn) are treated below.

The variations in the jet energy scale, the underlying event energy, and the $M_T^{e\nu}$ interval used in the fit described above should adequately account for any systematic errors in the shape of the W + 2 jet transverse mass distribution. However, as an independent check we estimate the systematic uncertainties due to these effects by directly modifying the transverse mass distribution of the W + 2 jet events. If the

Table 4.4: Summary of $\Delta\alpha$ for systematic effects for which the $M_T^{e\nu}$ distribution must be refit. The *Total* $\Delta\alpha$ column is the quadrature sum of the three effects.

M_{top} (GeV/c^2)	Jet Scale	Underlying Event	$M_T^{e\nu}$ Interval	Total $\Delta\alpha$
40	0.02	0.00	0.02	0.023
50	0.01	0.01	0.01	0.018
60	0.03	0.01	0.03	0.040
70	0.10	0.04	0.04	0.112
75	0.05	0.01	0.08	0.094
80	0.14	0.05	0.10	0.170

function $W(M_T^{e\nu})$ is too wide then there will be more $W^{\pm}$ events allowed at low $M_T^{e\nu}$, thereby reducing the amount of top needed in the fit. We artificially narrowed the $W(M_T^{e\nu})$ distribution and then refit to the data. The degree of narrowing was determined by fitting the transverse mass of the electron + 1 jet data transverse mass distribution to the W + 1 jet PAPAGENO prediction. A reduction in width of the electron + 1 jet $M_T^{e\nu}$ distribution of 3% corresponded a change in the log-likelihood of 1/2 unit in the fit to the W + 1 jet sample. This change in width was then applied to the W + 2 jet Monte Carlo sample and the resulting $M_T^{e\nu}$ distribution was fit to the $t\bar{t}$ Monte Carlo sample (M_{top} = 80 GeV/c^2) using the tight cuts. The result of

this fit

$$\alpha = 0.074^{+.367}_{-.074} \tag{4.9}$$

shows the variation in α to be within the range of the systematic error given above (Table 4.4).

4.2.2 Systematic uncertainties in normalization

The second category of systematic effects do not require refitting the transverse mass distributions. These effects, which may modify the acceptance in detecting $t\bar{t}$ or $W^{\pm}$ events, are

- the production properties of the top quark,
- the model of the fragmentation of a top quark into a hadron,
- the number of jets from initial state radiation,
- the modeling of the electron detection efficiency, and
- the integrated luminosity.

We have studied possible variations in $t\bar{t}$ production properties by comparing the ISAJET and PAPAGENO Monte Carlo calculations for $t\bar{t}$ production. The $t\bar{t}$ events are quite similar from these different calculations, the only significant difference being the softer p_T spectrum for top quarks in the PAPAGENO calculation, especially at low values of M_{top}. This difference in t quark p_T has no significant effect on the $M_T^{e\nu}$

distribution, given the kinematic cuts. The fitted value of α using the PAPAGENO $t\bar{t}$ transverse distribution for M_{top}=40 GeV/c^2 (the top mass for which there is the biggest discrepancy between PAPAGENO and ISAJET) does not differ significantly from the nominal fit result. However, this discrepancy does lead to a decrease in the $t\bar{t}$ acceptance for $M_{top} \lesssim 50$ GeV/c^2, for which we add a systematic error in the acceptance, shown in Table 4.5. For $M_{top} \geq 60$ GeV/c^2 the two calculations are in good agreement.

To model the fragmentation of partons, ISAJET uses the Peterson parametrization [24] of the fragmentation function, which is consistent with b and c quark data:

$$D_Q^H(z) = \frac{N}{z\left[1-(1/z)-\frac{\epsilon}{1-z}\right]^2}, \tag{4.10}$$

where $D_Q^H(z)$ is the probability that a heavy quark Q will form a hadron H with momentum fraction $z = p_H/p_Q$, ϵ is a parameter proportional to $1/M_Q^2$, and N is a normalization constant. To investigate the effect of a systematic uncertainty in the fragmentation model, we have varied ϵ in Eq. (4.10) from $0.2/M_{top}^2$ to $1.5/M_{top}^2$ (ISAJET's default value is $\epsilon = 0.5/M_{top}^2$). The only significant effect is on the isolation properties of electrons. The larger value of ϵ leads to a decrease in electron efficiency of 18% and 5% for 40 GeV/c^2 and 70 GeV/c^2, respectively. The shape of the $M_T^{e\nu}$ distribution is not significantly affected. The fractional decrease in $t\bar{t}$ acceptance is taken as the systematic uncertainty due to t quark fragmentation.

A comparison of jet activity in the inclusive electron sample with the b quark Monte Carlo sample has shown that the Monte Carlo reproduces the E_T spectrum and the rate of leading and non-leading jets (see Sec. 3.2.1). This implies that ISAJET's modeling of initial state radiation is fairly good. However, since the acceptance of $t\bar{t}$ events is sensitive to the number of jets arising from initial state radiation, we include as a systematic uncertainty the effect on the $t\bar{t}$ acceptance of varying the amount of initial state radiation. This change in acceptance was calculated by reselecting the $t\bar{t}$ Monte Carlo events with the additional requirement that all jets come from t quark (or $\bar{t}$ quark) decays. We then take half of this change as the fractional uncertainty in the $t\bar{t}$ acceptance due to uncertainty in the initial state radiation.

The uncertainty in the measured electron efficiency as compared to that reproduced by the Monte Carlo has been estimated to be $\pm 5\%$. This uncertainty covers the range of measured efficiencies determined from W and Z boson decays in the data. The integrated luminosity of the data sample is 4.4 pb^{-1}, with an uncertainty of $\pm 15\%$. A summary of these errors as a function of top mass is presented in Table 4.5.

4.3 Top mass limit

The fit results presented in Table 4.1 show no evidence for top quark production. Using these fit results we set an upper bound on the $t\bar{t}$ production cross section,

Table 4.5: Summary of systematic uncertainties in overall normalization. Values are expressed as fractions. The uncertainties summed in quadrature are listed in the Δn column.

M_{top} GeV/c^2	Production Model	Fragmentation Model	Initial State Radiation	Electron Efficiency	Integrated Luminosity	Δn
40	0.18	0.130	0.210	0.05	0.15	0.34
50	0.15	0.103	0.170	0.05	0.15	0.29
60	–	0.076	0.125	0.05	0.15	0.22
70	–	0.050	0.090	0.05	0.15	0.19
75	–	0.050	0.070	0.05	0.15	0.18
80	–	0.050	0.045	0.05	0.15	0.17

which is a function of M_{top}. We then compare these upper limits with the theoretically predicted $t\bar{t}$ production cross section to establish limits on the top quark mass.

We calculate the upper limit on the top cross section using the fitted value of α and its statistical and systematic uncertainties. We eliminate the necessity for making assumptions about the nature of the likelihood distribution for these fits by working with the full likelihood function. This is obtained by exponentiating and normalizing the log-likelihood function, which is determined by maximizing the value of the log-likelihood as a function of β, at a given value of α. Figure 4.4 shows this likelihood function for the 60 and 80 GeV/c^2 fits. The 95% confidence level (C.L.) upper limit on α is calculated by integrating this function after smearing it appropriately by the systematic uncertainty.

The systematic uncertainty has been divided into two parts as described above (Sec. 4.2). To see why this is necessary one must examine in more depth the meaning of the coefficient α. This coefficient has been defined as the fraction of the predicted $t\bar{t}$ cross section that is needed to fit the data. One may think of the fitting procedure as determining the number of $t\bar{t}$ events needed to fit the data. Then α may be written as

$$\alpha = \frac{n_{\text{obs}}}{n_{t\bar{t}}} = \frac{n_{\text{obs}}}{\epsilon \sigma_{t\bar{t}} \int \mathcal{L}\, dt} \tag{4.11}$$

where n_{obs} is the number of $t\bar{t}$ events needed to fit the data, $n_{t\bar{t}}$ is the number of $t\bar{t}$ events expected in the final sample, ϵ is the efficiency for detecting $t\bar{t}$ events, $\sigma_{t\bar{t}}$ is

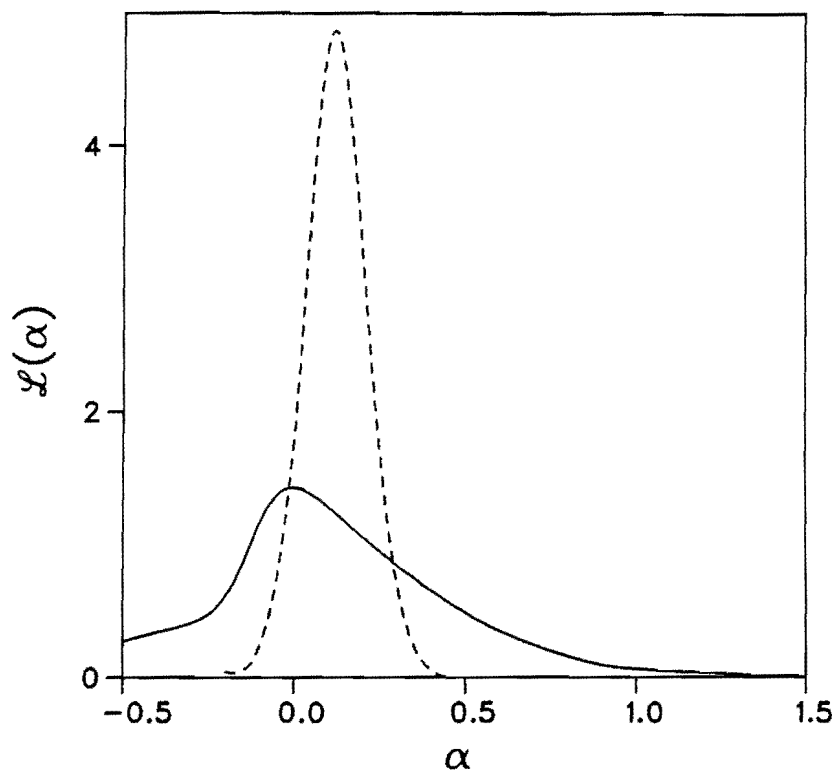

Figure 4.4: Normalized likelihood distributions for the 80 (solid curve) and 60 (dashed curve) GeV/c^2 fits.

the $t\bar{t}$ production cross section used in the Monte Carlo calculation, and $\int \mathcal{L}\, dt$ is the integrated luminosity. The numerator in this expression depends only on the $M_T^{e\nu}$ distribution of the data and on the shapes of the Monte Carlo distributions. The portion of the systematic error that requires refitting the $M_T^{e\nu}$ distribution, called $\Delta\alpha$ above, is the systematic error associated with $n_{\rm obs}$. This error must be expressed not as a fractional error in α (or $n_{\rm obs}$), but as an absolute error in the magnitude of α (or $n_{\rm obs}$). To see that this is true, one may consider the case when the fit gives α=0. Considering $\Delta\alpha$ as a fractional error would result in zero uncertainty in the number of $t\bar{t}$ events in the fit, a clearly erroneous result. The uncertainty in the overall normalization, Δn, derives from uncertainties in ϵ, the efficiency for detecting $t\bar{t}$ events, and in $\int \mathcal{L}\, dt$, the integrated luminosity.

The probability distribution is smeared according to its systematic uncertainty using a simple Monte Carlo program. First, a value of α, called α_0, is generated from the parent probability distribution obtained from the fit. Then the smearing due to $\Delta\alpha$ is applied by *adding* to α_0 a random number, whose parent distribution is Gaussian with mean zero and standard deviation $\Delta\alpha$. Then the smearing due to Δn is applied by *multiplying* by a number whose parent distribution is Gaussian with mean one and standard deviation Δn. This procedure is repeated one million times, yielding the smeared probability function for a given top mass, examples of which are shown in Fig. 4.5. This function is then integrated over the range $0 < \alpha < \infty$ and

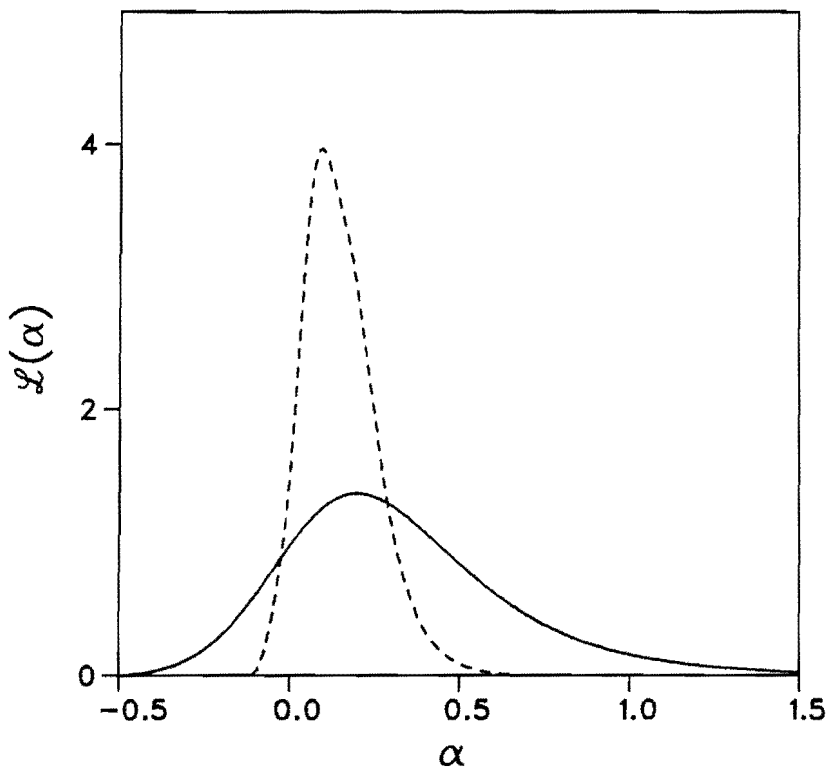

Figure 4.5: Smeared likelihood distributions for the 80 (solid curve) and 60 (dashed curve) GeV/c^2 fits.

Table 4.6: Summary of numbers used to calculate the upper limit on the $t\bar{t}$ production cross section. The theoretical prediction of Altarelli *et al.* ($\sigma_{t\bar{t}}$) and the lower bound on that calculation ($\sigma_{t\bar{t}}^{\min}$) are shown for comparison.

M_{top}					Theoretical	
(GeV/c^2)	$\alpha \pm$ (stat)	$\Delta\alpha$	Δn	$\sigma_{\max}$ (pb)	$\sigma_{t\bar{t}}$ (pb)	$\sigma_{t\bar{t}}^{\min}$ (pb)
40	0.07 ± 0.05	0.023	0.34	2410	9630	7130
50	0.06 ± 0.05	0.018	0.28	620	2930	2140
60	0.11 ± 0.08	0.040	0.22	408	1270	920
70	$0.00^{+0.12}_{-0.00}$	0.112	0.19	266	556	406
75	$0.00^{+0.18}_{-0.00}$	0.090	0.18	238	387	282
80	$0.00^{+0.27}_{-0.00}$	0.170	0.17	281	285	208

normalized to unity to determine the value of α, denoted $\alpha_{\max}$, above which lies 5% of the area under the probability curve. This is the 95% C.L. upper limit for α. The 95% C.L. upper limit on the $t\bar{t}$ cross section derived from the fit is then

$$\sigma_{\max} = \sigma_{t\bar{t}}\, \alpha_{\max}. \tag{4.12}$$

We emphasize that this upper limit on the cross section is independent of any theoretical prediction of the $t\bar{t}$ production cross section. This procedure is repeated for each value of M_{top}, yielding an upper limit on the $t\bar{t}$ cross section as a function of t quark mass. Table 4.6 summarizes this calculation.

To verify this procedure for arriving at the 95% C.L. upper limit for the $t\bar{t}$ cross section we have repeated the procedure for a large number of Monte Carlo generated experiments. For each "experiment," a transverse mass distribution containing a mixture of $t\bar{t}$ and W + 2 jet events is generated. The number of $t\bar{t}$ events in this mixture was chosen to correspond to the 95% C.L. upper limit on the observed cross section (σ_{max} in Table 4.6). The number of W + 2 jet events was fixed by requiring that, on average, the total number of events in the Monte Carlo experiment be equal to the number of electron + 2 jet events in the real data (i.e., 104 events for the tight cuts and 123 for the loose cuts). The transverse mass for the $t\bar{t}$ and W + 2 jet events were distributed according the the functions $T(M_T^{e\nu})$ and $W(M_T^{e\nu})$, respectively. This transverse mass distribution is then fit as the data was. The resulting value of α is then smeared by the appropriate values of $\Delta\alpha$ and Δn, first by adding a number generated from a Gaussian distribution of mean zero and width $\Delta\alpha$, and then by multiplying the result by a number generated from a Gaussian distribution with mean one and width Δn. The result is the value of α obtained from one experiment. This procedure is repeated 1000 times, resulting in 1000 values of α. If the number of times that α is less than value of α obtained when fitting the real data is denoted n', then the confidence level for excluding the $t\bar{t}$ cross section used (σ_{max}) is given by

$$C.L. = 1 - \frac{n'}{1000}. \tag{4.13}$$

The confidence level obtained in this manner for each top mass is shown in Table 4.7.

Table 4.7: Alternate determination of the confidence level of the quoted upper limit of the $t\bar{t}$ cross section as described in the text.

M_{top} (GeV/c^2)	C.L.
40	97.8
50	98.1
60	97.9
70	97.3
75	97.7
80	98.2

The confidence levels obtained in this manner are consistent with each other but systematically higher than those obtained using the likelihood function determined from the fit to the data. This difference can be understood by noticing that the likelihood distributions are not symmetric: the tail at higher values of α is longer than the tail at lower values of α. Our first method of determining the confidence level essentially considers the area under the likelihood curve *above* a given value of α (i.e., in the longer tail), while the second method considers the number of times α falls *below* a particular value (in the shorter tail). This study indicates that the 95% C.L. upper limit cross sections shown in Table 4.6 may be slightly conservative.

Figure 4.6 shows the upper limit on the observed top quark cross section as a function of top mass. The two solid curves are produced by performing the analysis with the loose and tight kinematic cuts. The region above these curves is excluded at 95% C.L. We compare these curves with a calculation of the $t\bar{t}$ production cross section by Altarelli *et al.* [4]. This calculation is based on the QCD total cross section formulas for heavy quark production, complete through order α_s^3, by Nason *et al.* [17]. The shaded region represents the theoretical uncertainty in the calculation based on various choices of the renormalization scale, μ,and the QCD scale parameter, Λ_s. The points of intersection of the solid curve with the lower edge of the shaded band show that the top quark is excluded at 95% C.L. for

$$40 < M_{top} < 77 \text{ GeV/c}^2. \tag{4.14}$$

The systematic uncertainties on jet detection efficiency and top fragmentation grow rapidly with decreasing M_{top}, so we do not extend the lower mass limit below 40 GeV/c^2.

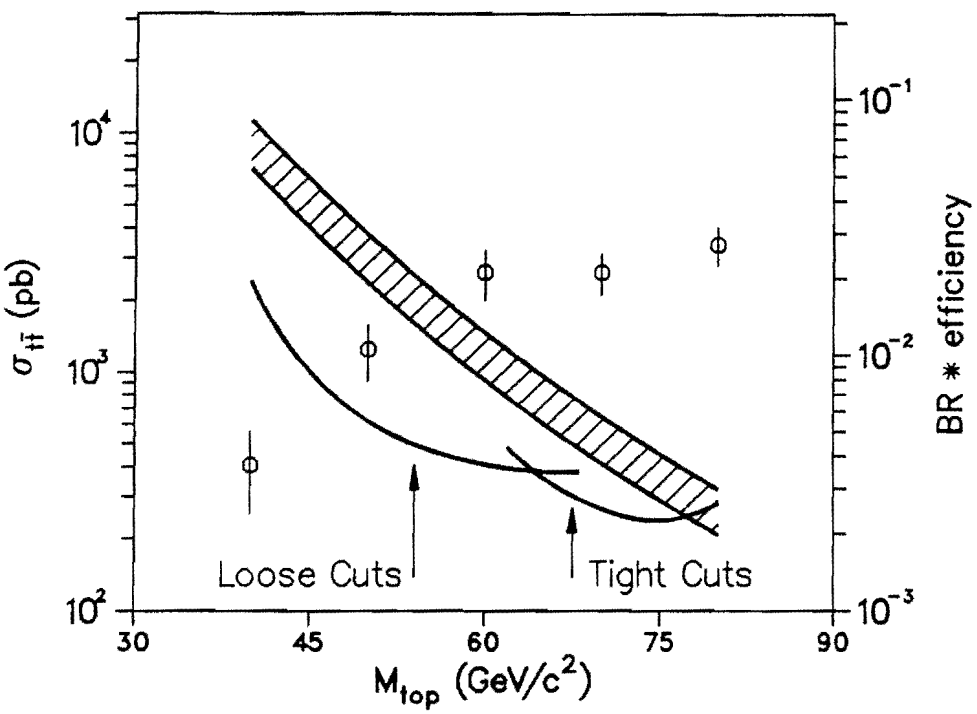

Figure 4.6: The 95% C.L. upper limit for the $t\bar{t}$ production cross section as a function of top mass is given by the solid curves. The shaded region gives the predicted $t\bar{t}$ cross section (see text). The plotted points show the $t\bar{t}$ efficiency as a function of M_{top} (right-hand scale).

Chapter 5

Conclusions

Based on an analysis of events with a high-p_T electron, significant $\not\!\!E_T$, and two or more jets with $E_T > 10$ GeV, we have excluded at 95% confidence level the existence of a standard model top quark in the range $40 < M_{top} < 77$ GeV/c^2. This mass limit is based on the reaction $\bar{p}p \rightarrow t\bar{t}+X$ and therefore depends on the theoretical prediction of the cross section for this process. The analysis also depends on the standard model prediction for the semileptonic branching ratio of 1/9 for the top quark. Given these assumptions, the 77 GeV/c^2 limit is the strongest limit on the top quark mass to date, however there exist weaker limits from e^+e^- colliders ($M_{top} \gtrsim 45$ GeV/c^2) that are not subject to these theoretical conditions.

5.1 Consistency with indirect constraints

The top quark mass limits obtained in this analysis are consistent with indirect limits obtained from $B^0\bar{B}^0$ mixing results and from analysis of weak neutral current data. Within the context of the Standard Model, both of these results indicate that the top

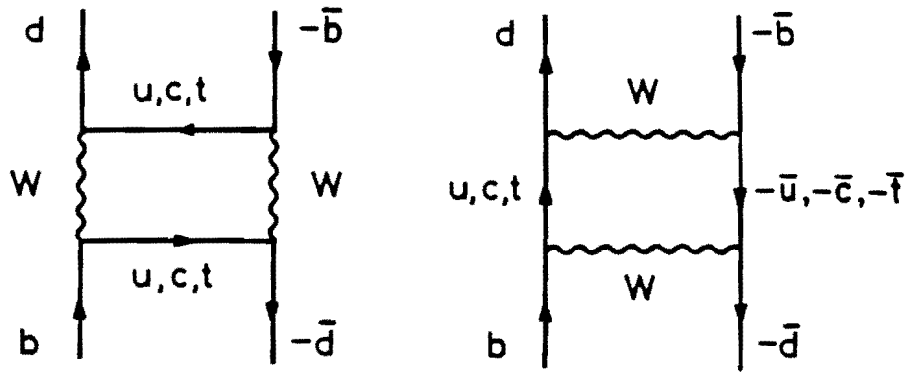

Figure 5.1: Box diagrams contributing to $B^0\bar{B}^0$ mixing

quark is heavier than about 50 GeV/c^2, and furthermore that the top quark is likely to be heavier than the W boson.

5.1.1 $B^0\bar{B}^0$ mixing

The charged current term of the electroweak Lagrangian (Eq. (1.4)) allows mixing in the $B^0\bar{B}^0$ system via the box diagrams of Fig. 5.1, where the internal quark lines can be u, c, or t quarks [25]. Mixing is parametrized by the quantity

$$r \equiv \frac{P(B^0 \to \bar{B}^0)}{P(B^0 \to B^0)} \tag{5.1}$$

which has been measured to be [9]

$$r_d = 0.21 \pm 0.08, \tag{5.2}$$

where the subscript d refers to mixing among B_d^0 mesons. Within the Standard Model with three families of leptons and quarks the quantity r can also be expressed as

$$r = \frac{x^2 + y^2}{2 + x^2 - y^2} \simeq \frac{x^2}{2 + x^2}, \tag{5.3}$$

where $x = \Delta M/\Gamma$, $y = \Delta\Gamma/2\Gamma$ and ΔM and $\Delta\Gamma$ are the mass and width differences between the long and short lifetime mass eigenstates. Γ is the average width of the two states. The t quark contribution dominates x_d and one finds

$$x_d \simeq \frac{G_F^2}{6\pi^2}\tau_B B_B f_B^2 m_B |V_{td}V_{tb}^*| \frac{A(z)}{z}\eta_t m_{top}^2, \tag{5.4}$$

where G_F is the Fermi constant, τ_B is the B_d lifetime, $B_B f_B^2$ is determined by evaluating $\langle B_d^0|J_\mu^\dagger J^\mu|B_d^0\rangle$, $m_B = 5.275$ GeV/c^2 is the B_d mass, and V_{ti} are the Cabbibo-Kobayashi-Maskawa (CKM) matrix elements. The function $A(z)/z$ ($z = m_{top}^2/M_W^2$) is a slowly varying function that varies from 1–0.75 in the range $0 < M_{top} < M_W$, and $\eta_t = 0.85$ is a QCD correction factor. For a wide range of M_{top} centered on $M_{top} = 40$ GeV/c^2 Eq. (5.4) can be written as

$$x_d \simeq .15 \left(\frac{\tau_B |V_{td}|^2}{3.3 \times 10^{-16}\ \mathrm{s}}\right)\left(\frac{B_B f_B^2}{(.14\ \mathrm{GeV})^2}\right)\left(\frac{M_{top}}{40\ \mathrm{GeV/c^2}}\right)^2. \tag{5.5}$$

The CKM matrix element V_{td} is not well known, but it is constrained by unitarity and its relation to other known CKM elements. Based on limits on $\Gamma(b \to u)/\Gamma(b \to c)$,

the b lifetime and the semileptonic branching ratio for b decays, one finds

$$\tau_b |V_{tb}|^2 = (0.02 \text{ to } 6.2) \times 10^{-16} \text{ s}. \tag{5.6}$$

The value of $B_B^{1/2} f_B$ has been estimated using theoretical techniques and also by extrapolating experimental results on charm quark decay. One finds

$$B_B^{1/2} f_B = (140 \pm 40) \text{ MeV}. \tag{5.7}$$

Taking the central values for $\tau_B |V_{td}|^2$ and $B_B f_B^2$ along with the Argus result ($x_d = 0.73 \pm 0.18$), Eq. 5.5 implies that $M_{top} \gtrsim 90$ GeV/c^2. Increasing the values for $\tau_B |V_{td}|^2$ and $B_B f_B^2$ to 6×10^{-16} s and (180 MeV)^2 respectively, yields $M_{top} \gtrsim 45$ GeV/c^2.

Thus, within the context of the Standard Model with three generations of quarks and leptons, the measured value of $B^0 \bar{B}^0$ mixing implies $M_{top} \gtrsim 45$ GeV/c^2.

5.1.2 Neutral current data and vector boson masses

The mass of the top quark is also constrained by experimental results on weak neutral current processes and the vector boson masses [26]. Radiative corrections to $\mathcal{O}(\alpha)$ depend on M_{top} and (to a lesser extent) on M_H, the mass of the Higgs boson. This is illustrated most clearly in the radiative-corrected expression for the mass of the Z^0 boson [27]

$$\begin{aligned} M_Z &= \frac{2A}{\sin 2\theta_W}, \\ A &\equiv \left[\frac{\pi\alpha}{\sqrt{2}G_F}\right]^{\frac{1}{2}} \left[\frac{1}{1-\Delta r}\right]^{\frac{1}{2}} \end{aligned} \tag{5.8}$$

Table 5.1: Dependence of radiative corrections, Δr, on the top quark mass (from ref. [27]). These values were calculated using $\sin^2\theta_W = 0.217$ and $M_H = M_Z$. Also shown is the value of A from Eq. (5.8).

M_{top} (GeV/c^2)	Δr	A (GeV/c^2)
20	0.0699	38.66
36	0.0696	38.65
60	0.0714	38.69
83	0.0623	38.50
100	0.0558	38.37
150	0.0379	38.01
200	0.0167	37.60
240	−0.00355	37.21

$$= \frac{37.2810 \pm .0003 \text{ GeV}}{(1-\Delta r)^{1/2}}.$$

Here Δr denotes the $\mathcal{O}(\alpha)$ radiative corrections. In this renormalization scheme, the weak mixing angle is defined by

$$\sin^2\theta_W \equiv 1 - \frac{M_W^2}{M_Z^2}. \tag{5.9}$$

The dependence of Δr on M_{top} is shown in Table 5.1. One sees that a precise determination of M_Z will give Δr (from Eq. (5.8)), and hence M_{top} (from Table 5.1),

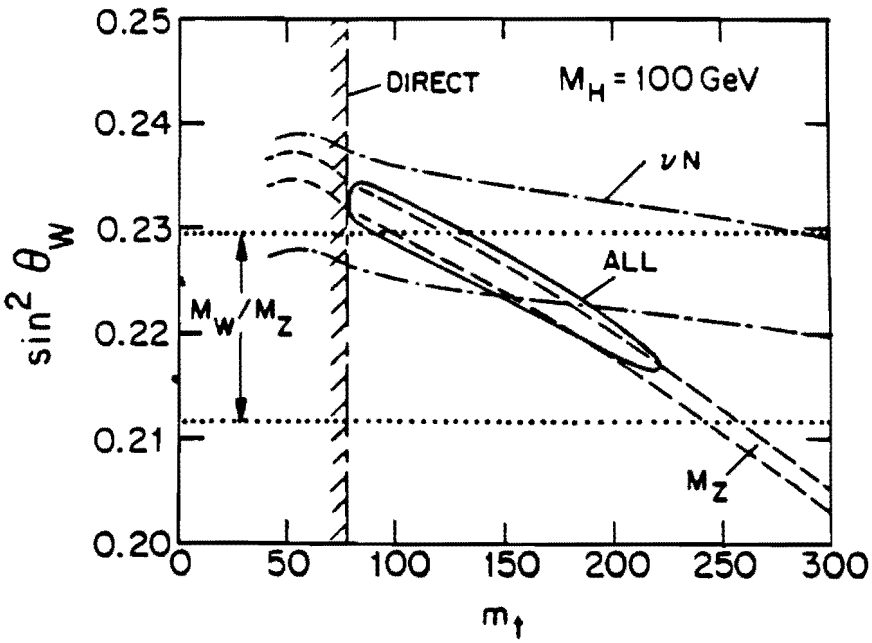

Figure 5.2: $\pm 1\sigma$ uncertainties in $\sin^2\theta_W \equiv 1 - M_W^2/M_Z^2$, determined from M_Z (dashed line), M_W/M_Z (dotted line), and νN neutral current data (dash-dotted line) as a function of M_{top} for $M_H = 100$ GeV/c^2. Also shown is the direct lower limit from the nonobservation of the t quark in $\bar{p}p \to t\bar{t} + X$ (long-short line), and the region (solid line) in $\sin^2\theta_W$-M_{top} allowed by all data at 90% CL ($\Delta\chi^2 = 4.6$).

for a particular choice of $\sin^2\theta_W$. Furthermore, a measurement of the ratio M_W/M_Z yields a value of $\sin^2\theta_W$ that is independent of M_{top} (see Eq. (5.9)). A third important measurement, that of νN scattering, also has an M_{top} dependence via radiative corrections, but the functional dependence is different than for the M_Z or M_W/M_Z measurements. Combining these measurements eliminates certain regions of the $\sin^2\theta_W$–M_{top} plane. This is shown in Fig. 5.2, which is taken from ref. [28]. A Higgs mass of 100 GeV/c^2 is assumed in this figure. Also shown is a preliminary

version of the direct top quark mass limit presented in this paper. The curves in this figure are based on the following results, which were the best available at the time [29]:

- $M_Z = 91.17 \pm 0.18$ GeV/c^2,
- $M_W/M_Z = .883 \pm .005$, and
- $M_{top} > 78$ GeV/c^2 at 90% C.L.

A two parameter fit of these data and others, including results from atomic parity violation, from the polarized *ed* asymmetry, and from $\nu_\mu e$ scattering, yields

$$\sin^2\theta_W = 0.226 \pm .005, \tag{5.10}$$

and

$$M_{top} = 140^{+43}_{-52} \text{ GeV/c}^2. \tag{5.11}$$

Even without the direct limit on M_{top}, the data constrain M_{top} to be greater than 50 GeV/c^2 at 90% C.L. This weaker limit is not subject to the constraint that $t \to Wb$ be the dominant decay mode of the top quark.

The prospect for further constraining the mass of the top quark via its effect on electroweak radiative corrections in the near future is not very promising. The more recent and precise results on M_Z now available from the LEP experiments do not significantly further constrain the values of M_{top} and $\sin^2\theta_W$. A measurement of the

left-right asymmetry (A_{LR}) using polarized beams at SLC or LEP could possibly yield some further constraint. A very precise measurement of M_W from $\overline{p}p$ colliders or from LEP-II would also be significant, reducing the relatively large error on M_W/M_Z.

If the top quark were discovered and its mass measured, one might think of constraining the mass of the Higgs boson using the radiative corrections. Unfortunately, this is not practical given the weak dependence of Δr on M_H. Given the precision of current and proposed experiments at LEP, little will be learned about M_H using radiative corrections (although, of course, much can be learned via direct Higgs searches at e^+e^- colliders).

5.2 Future prospects

We comment briefly on the prospect of finding the top quark in future searches. It is apparent that the decay mode $Z^0 \to t\bar{t}$ is ruled out, and with it the possibility of observing the top quark at SLC or LEP-I. The decay mode $W \to t\bar{b}$ is now also ruled out (given the theoretical assumptions described above), and the cross section for direct production of $t\bar{t}$ pairs at $\sqrt{s} = 630$ GeV is small enough to make the prospect of discovering top at the CERN $\overline{p}p$ collider doubtful. There is still a small window of mass available for the discovery of the top quark at LEP-II, but it is not likely to be found there.[1] The top quark should be observable in data from the 1991 run of

[1]The CDF collaboration announced on March 1, 1990 a new limit on the top quark mass: $M_{top} >$ 89 GeV/c^2 at 95% C.L., obtained by combining several top quark decay channels.

the Fermilab Tevatron if $M_{top} \lesssim 130$ GeV/c^2. A later run scheduled for 1994 should be sensitive to top masses up to about 180 GeV/c^2. If the top quark has not been discovered by then, future hadron colliders such as the SSC or LHC will probe top quark masses up to about 1 TeV/c^2.

Chapter 6

Bibliography

[1] F. Abe *et al.*, CDF collab., Phys. Rev. Lett. **64**, 142 (1990).

[2] T. Kamae, Proceedings of the XXIV International Conference on High Energy Physics, edited by R. Kotthaus and J. Kuhn, Springer-Verlag (1989), p. 156.

[3] C. Albajar *et al.*, UA1 collab., Z. Phys. bf C37 505, (1984);
I. J. Kroll, Proceedings of the XXIV International Conference on High Energy Physics, edited by R. Kotthaus and J. Kuhn, Springer-Verlag (1989), p. 1416.

[4] G. Altarelli, M. Diemoz, G. Martinelli and P. Nason, Nucl. Phys. **B308**, 724 (1988).

[5] T. Åkesson *et al.*, UA2 collab., CERN-EP/89-152 (1989);
D. Decamp *et al.*, ALEPH collab., CERN-EP/89-165 (1989). The limit quoted in this paper is $M_{top} > 45.8$ GeV/c^2;
M. Akrawy *et al.*, OPAL collab., CERN-EP/89-154 (1989).

[6] See, for example, C. Quigg, *Gauge Theories of the Strong, Weak, and Electromagnetic Interactions* (Benjamin/Cummings, Reading, Mass. 1983).

[7] A recent summary of asymmetries is given in C. Kiesling, *Electroweak Tests of the Standard Model* (Springer-Verlag, Berlin 1988).

[8] W. Bartel *et al.*, JADE collab., Phys. Lett. **146B**, 437 (1984).

[9] H. Albrecht *et al.*, ARGUS collab., Phys. Lett. **192B**, 245 (1987).

[10] G. L. Kane and M. Peskin, Nucl. Phys. **B195**, 29 (1985).

[11] A. Bean *et al.*, CLEO collab., Phys. Rev. **D35**, 3533 (1987).

[12] F. Abe *et al.*, CDF collab., Phys. Rev. Lett. **64**, 147 (1990).

[13] S. Glashow and E. Jenkins, Phys. Lett. **196B**, 233 (1987).

[14] F. Abe *et al.*, CDF collab., Nucl. Instr. Meth. **A271**, 387 (1988).

[15] F. Abe *et al.*, CDF collab., Phys. Rev. Lett. **62**, 3020 (1989).

[16] F. Paige and S. D. Protopopescu, BNL Report No. BNL 38034, 1986 (unpublished). The $b\bar{b}$ and $t\bar{t}$ event samples were generated with version 6.10 and 6.21, respectively.

[17] P. Nason, S. Dawson and R. K. Ellis, Nucl. Phys. **B303**, 607 (1988).

[18] I. Hinchliffe, in preparation. Version 2.71 of PAPAGENO was used for the W + jets calculations.

[19] R. K. Ellis and R. J. Gonsalves, Proceedings of the Supercollider Physics Topical Conference, edited by D. Soper, World Scientific (1985), p. 287.

[20] J. Rosner, Phys. Rev. **D39**, 3297 (1989).

J. Rosner, Phys. Rev. **D40**, 1701 (1989).

H. Baer, V. Barger, and R. J. N. Phillips, Phys. Lett. **B221**, 398 (1989).

[21] F. E. James and M. Roos, Comput. Phys. Commun. **10**, 343 (1975).

[22] The Particle Data Group, G.P. Yost *et al*, Phys. Lett. **B204**, 74 (1988).

[23] M. Mangano and S. Parke, Fermilab Pub 89/106-T (July, 1989).

[24] C. Peterson, D. Schlatter, I. Schmidt and P. Z. Zerwas, Phys. Rev. **D27**, 105 (1983).

[25] In this section, we follow the analysis of G. Altarelli and P. J. Franzini, Z. Phys. **C37**, 271 (1988).

[26] A full analysis of electroweak radiative corrections and experimental results can be found in U. Amaldi *et al.*, Phys. Rev. **D36**, 1385 (1987).

[27] W. J. Marciano and A. Sirlin, Phys. Rev. **D29**, 945 (1984).

[28] P. Langacker, Phys. Rev. Lett. **63**, 1920 (1989).

[29] G. Feldman, MARK-II collab., in Proceedings of the Fourteenth International Symposium on Lepton and Photon Interactions, Stanford, California, August 1989 (to be published).

M. Campbell, CDF collab., in the same proceedings.

A. Weidberg, UA2 collab., in the same proceedings.

P. Sinervo, CDF collab., in the same proceedings.